Forward Modeling of Active Region Coronal Emissions. I. Methods and Testing

2008 ApJS 179 509

(http://iopscience.iop.org/0067-0049/179/2/509)

THE ASTROPHYSICAL JOURNAL SUPPLEMENT SERIES, 179:509–533, 2008 December

FORWARD MODELING OF ACTIVE REGION CORONAL EMISSIONS. I. METHODS AND TESTING

L. L. LUNDQUIST[1,2]
Harvard-Smithsonian Center for Astrophysics, 60 Garden St. MS-58, Cambridge, MA 02138; llundquist@cfa.harvard.edu

AND

G. H. FISHER AND J. M. MCTIERNAN
Space Sciences Laboratory, University of California, Berkeley, CA 94720-7450

Received 2007 April 8; accepted 2008 April 2

ABSTRACT

We present a method for simulating coronal emissions from solar active regions using observed photospheric magnetograms and an assumption about the coronal heating mechanism as input. The method invokes a "quasi–force-free" (minimized Lorentz force) coronal magnetic solution and a steady state energy balance model solved along field lines. Coronal heating is included using parameterized approximations relating the heat deposited to properties of the magnetic field. We use calculated temperatures and densities to predict emissions and compare to observations from the *Yohkoh* Soft X-ray satellite. We use NOAA active region 8210 to test the model's sensitivities. We find predicted intensities and emission morphologies change little with different assumptions for the coronal magnetic field. We test methods for calculating the proportionality constant in a heating scale relationship and find filling factors of $\sim(1-5)\times10^{-2}$ are needed to match temperature in the cases considered. We investigate the effect of heating scale height, finding that loop-top heating improves temperature predictions but decreases success of the emission morphology prediction. Footpoint heating has the opposite effect. Overall, our model produces relatively robust results for a wide range of assumptions. Yet the results are highly sensitive to the input coronal heating parameterization, making our method a powerful approach for discriminating between heating mechanisms. Nevertheless, we find substantial discrepancies between our synthetic emissions and observed emissions. We investigate sources of discrepancy and suggest that improved magnetic field extrapolations and dynamic heating are necessary to improve simulations.

Subject headings: Sun: corona — Sun: magnetic fields — Sun: X-rays, gamma rays

Online material: color figures

1. INTRODUCTION

More than three decades of space-based X-ray, extreme-ultraviolet (EUV), and UV observations of the Sun's corona have offered an unprecedented view of the solar atmosphere of active regions. Understanding the physics of these active-region coronae is a fundamental goal in the field of solar physics and studies of the Sun-Earth connection. A first step in this pursuit is an understanding of coronal equilibrium configurations.

The observations reveal that arched, magnetic-field–associated "coronal loops" are the building blocks of the solar corona. Rosner et al. (1978) and Craig et al. (1978) were the first to show that these loops could be modeled individually, approximated as one-dimensional structures thermally and mechanically isolated from their surroundings. Their model assumed symmetric, semicircular loops in static equilibrium, unaffected by gravity, with uniform cross-sectional area and uniform heating profiles from an unknown heating mechanism. Later studies of equilibrium loops relaxed some of these assumptions (see e.g., Cargill & Priest 1980; Landini & Monsignori Fossi 1981; Serio et al. 1981; Wragg & Priest 1981; Wallenhorst 1982; Mariska & Boris 1983; Craig & McClymont 1986; Steele & Priest 1990, 1991; Peres et al. 1992; Orlando et al. 1995; Aschwanden & Schrijver 2002).

These equilibrium models have done relatively well at explaining many observed soft X-ray loops (Rosner et al. 1978; Porter & Klimchuk 1995; Kano & Tsuneta 1996; Kankelborg et al. 1997), although they have largely failed at describing cooler EUV loops observed by recent narrowband instruments (Lenz et al. 1999; Lenz 1999; Aschwanden et al. 2000, 2001; Winebarger et al. 2003; Patsourakos et al. 2004). Comparing these models to observations reveals a number of difficulties. (1) Selection effects are ubiquitous, with loops that are easiest to observe being brightest (and brighter than background emission), isolated from other loops, and visible along most or all of their length. These may not be representative of typical coronal loops. (2) Loop observations are necessarily a two-dimensional projection of a three-dimensional plasma structure, evoking interpretation issues for both geometry and emission. Geometrically, the exact position and orientation of coronal structures can be misleading. Loop emission measures will include emission from plasma in front of and behind the loop, along the observation line of sight. Background subtraction can eliminate some of these concerns, if a suitable background is found, but again, this can be misleading (see e.g., Reale 2002; Del Zanna & Mason 2003; Schmelz et al. 2003, 2005; Ugarte-Urra et al. 2005).

An alternative to studying individual loops is to model an entire active region corona in three dimensions. Magnetohydrodynamic (MHD) modeling forms the bulk of this effort. Because they are three-dimensional, comparing these models with data does not entail any of the difficulties mentioned above. However, these studies are highly computationally expensive, particularly if the energy equation, critically important for determining the thermodynamic properties of the corona, is treated in full. Furthermore, many of these studies are performed from idealized initial conditions and cannot be compared directly with coronal data from a specific region, but rather apply to all regions in a more

---

[1] Space Sciences Laboratory, University of California, Berkeley, CA 94720-7450.

[2] The Institute of Space and Astronautical Science, Sagamihara 229, Japan.

qualitative sense. Finally, most three-dimensional MHD models in current use employ extremely simplified versions of the energy equation because of computational limitations, although progress is being made toward improving these calculations (see, e.g., Lionello et al. 2003).

There is a middle ground between the studies of individual loop models and three-dimensional MHD calculations with full treatment of the energy equation that has not been covered adequately. In this paper we present an approach to model active region coronae without requiring a great deal of computational resources. It consists of simply building up an entire active region from its internal building blocks, the coronal loops. We model each loop separately with one-dimensional steady state energy balance models, attempting to select a representative and (mostly) spatially filling set of loops. The basis for the loop models is the result of a magnetic field extrapolation from magnetic field observations of the region. Temperature and density results from the loop calculations are interpolated to a regular three-dimensional grid. The result is an equilibrium representation of a full active region.

An important advantage of the method is that it enables the creation of synthetic emission images. These represent a prediction of the emission measure per pixel of an active region, which can be compared to actual emission measures to determine success of the model. This eliminates both selection effects and projection difficulties involved with individual loop comparisons while retaining the ability to compare quantitatively with data, as well as keeping parameter space and computational effort to a minimum. In this paper, we consider the merits of various ways to compare synthetic images to the observations.

Since our initial presentations (Lundquist et al. 2003a, 2003b, 2004a, 2004b, 2005; Lundquist 2006a, 2006b) of the forward modeling approach described here, similar techniques have been adopted by a number of other researchers. Schrijver et al. (2004) perform full-Sun forward modeling using a potential field extrapolation and a static loop model. Mok et al. (2005) model active regions with a force-free extrapolation and a three-dimensional MHD model with heating rate proportional to magnetic field strength. Warren & Winebarger (2007) focus on active regions and use a similar parameter space as ours, with a potential field extrapolation and a static loop model. In Warren & Winebarger (2007), the same authors begin to extend this framework to dynamic loop modeling. We compare the results of these studies to our own results in Lundquist et al. (2008; hereafter Paper II).

In this paper, we also test extensively the assumptions of our method, focusing on NOAA-designated region 8210 (AR 8210) as a case study. This region, observed on 1998 May 1, has been studied extensively in the literature as well as being the focus of two major joint studies as a Solar, Heliospheric and Interplanetary Environment (SHINE) Campaign Event[3] and the focus of the Solar MURI project.[4] A partial list of relevant papers addressing this region includes: Régnier et al. (2005), Barnes et al. (2005), Welsch et al. (2004), Longcope (2004), Roussev et al. (2004); Leka & Barnes (2003); Wang et al. (2002), Simnett (2002), Sterling & Moore (2001b), Sterling et al. (2001), Sterling & Moore (2001a), Pohjolainen et al. (2001), Thompson et al. (2000), and Warmuth et al. (2000).

We choose this region primarily for the quality of data available, the distinctive appearance of its coronal X-ray emissions, and the extensive previous research. The data available include excellent vector magnetogram measurements that coincide temporally with full resolution images from the *Yohkoh* Soft X-ray telescope, an instrument whose broadband pass provides the best coverage of overall coronal emissions.

We describe our method in § 2, including some variations available for different applications. In § 3, we present the results of our magnetic field modeling and loop calculations. In § 4 we present the predicted emissions from AR 8210 using four different assumed coronal heating parameterizations. This section includes an exploration of the options available for quantitative comparison of the predicted images with the observations (§ 4.2). Further sections explore the impact of different assumptions on the predicted emissions. In § 5 we examine the effects of changing the magnetic field extrapolation method and the field line representation of the coronal magnetic field solution. In § 6 we focus on the effects of assumptions that go into our loop model solutions, including choices of the volumetric filling factor, the distribution of heat deposition along the loop, elemental abundances in the corona, and thermal conduction. We summarize our conclusions in § 7.

2. METHOD

A short overview of our method follows. The primary input to the model is a three-dimensional data cube of coronal vector magnetic field values. Such a data set can be created through a number of different methods (§ 2.1.1). We begin by calculating a set of magnetic field lines from these data. Next, we solve a steady state energy equation along each loop to determine thermodynamic variables, which requires an expression for the amount of heat input due to an assumed coronal heating mechanism (§ 2.2). We discuss the numerical details of the energy calculation in this same section. Once temperature and density solutions are achieved along every loop, we interpolate these thermodynamic variables from the coronal loops to a three-dimensional grid (§ 2.3). We create synthetic emission images of the region by integrating emissivity over line of sight and convolving with instrument response function (§ 2.4). Results from this type of calculation for AR 8210 are presented in § 3, along with a comparison with the observed *Yohkoh* Soft X-ray Telescope images (Tsuneta et al. 1991) taken of this active region at times near to the original magnetogram data.

2.1. *The Magnetic Field*

2.1.1. *Generating an Input Coronal Field*

Our method requires three-dimensional vector information about the coronal magnetic field. Because coronal field measurement techniques are still being developed (e.g., Brosius et al. 2002; Lin et al. 2004; Brosius & White 2006) and do not provide full three-dimensional information, we must adopt a method to solve for a coronal magnetic field. Many options exist, such as extrapolations from two-dimensional data (e.g., photospheric or chromospheric magnetograms) via potential or force-free field solutions, or output from an MHD simulation. Computing the magnetic field separately from the thermodynamics involves the implicit assumption of a low-β corona (see, e.g., Gary 2001 for a discussion of plasma β-values in active-region coronae).

In the example presented in this paper, we use the nonconstant α "quasi" force-free-field calculation described in Wheatland et al. (2000). "Nonconstant α" refers to the α that relates the current density, $\boldsymbol{j}$, to the magnetic field, $\boldsymbol{B}$, in the force-free assumption where $\boldsymbol{j} \times \boldsymbol{B} = 0$ and $\boldsymbol{j} = \alpha \boldsymbol{B}$. Our solution allows α to vary across different field lines throughout the active region.

---

[3] Available online at http://www.shinegroup.org/campaign.html.

[4] Available online at http://sprg.ssl.berkeley.edu/home/yanli/public_html/muri/events98.html.

The technique minimizes the global departure of an initial field from a force-free and solenoidal state. Our initial guess for the field in the coronal volume is a potential-field extrapolation of the photospheric magnetic data. In the sense that the Lorentz force $(\nabla \times \boldsymbol{B}) \times \boldsymbol{B}$ is minimized and may not be strictly zero at every point in the volume, we refer to the solution as "quasi–force-free."

The following boundary conditions are employed: at the bottom box boundary, the field is set equal to the measured photospheric magnetic field, and the field at the other boundaries of the box is set equal to the results of the initial potential field solution.

The Wheatland et al. (2000) method, also known as the "optimization" method, compares favorably with other nonlinear force-free extrapolation methods (Schrijver et al. 2005, 2006). An advantage of the method is that it allows the use of all of the measured data, unlike the strictly force-free field solution, which is overprescribed if all of the information about the measured field at the bottom boundary is imposed. This overprescription is avoided, because the optimization technique allows the field to remain non–force-free near the photosphere, as it typically is on the Sun (e.g., Metcalf et al. 1995), requiring only that it be as force-free as possible. A disadvantage is that the solution is not guaranteed to be completely solenoidal ($\nabla \cdot \boldsymbol{B} = 0$); it only requires that the sum of the squares of the force and divergence is minimized. In practice, however, the solution is relatively divergence free (§ 3.2).

2.1.2. *Choosing Field Lines*

Using the input coronal field, we calculate a set of magnetic field lines to represent the field. Field lines are integrated up from the photosphere, starting from every pixel of the magnetogram with $|\boldsymbol{B}|$ larger than a threshold value. Of the resulting lines, we associate the field lines that close within the box with coronal loops for which we can solve an energy equation (§ 2.2). Field lines that close on box boundaries other than the bottom of our extrapolated coronal field are considered "open." Because our loop model applies only to closed loops, we are forced to ignore these open loops, with the implicit assumption that they make a negligible contribution to the total emission of the active region. "Open" loops tend to be longer and thus cooler (assuming a heating rate that varies with loop length raised to a power of 2 or less [Rosner et al. 1978], as most predicted heating mechanisms do [Mandrini et al. 2000]). Thus, they will be less likely to contribute substantially to the emission. Nevertheless, our model clearly applies best to active regions with (1) flux balance in the magnetogram measurements, and (2) no strongly emitting loop connections to nearby regions or to flux systems outside the field of view of the magnetic field measurements.

Our interpolation procedure (§ 2.3) helps to eliminate some dependence on which field lines are chosen to represent the active region. Section 5.2 discusses the sensitivity of the solution to the field lines chosen to represent the active region.

2.2. *Loop Solutions*

The basic equations for calculating loop thermodynamics are the MHD equations for conservation of mass, momentum, and energy,

$$\frac{\partial \rho}{\partial t} + \nabla \cdot \rho \boldsymbol{v} = 0, \tag{1}$$

$$\rho \frac{D\boldsymbol{v}}{Dt} + \nabla P - \boldsymbol{j} \times \boldsymbol{B} - \rho \boldsymbol{g} = 0, \tag{2}$$

$$\frac{3}{2}\frac{DP}{Dt} - E_H + E_R + \nabla \cdot \boldsymbol{F}_C + \frac{5}{2} P \nabla \cdot \boldsymbol{v} = 0, \tag{3}$$

where t is time, ρ is mass density, $\boldsymbol{v}$ is plasma velocity, P is gas pressure, $\boldsymbol{j}$ is current density, $\boldsymbol{B}$ is magnetic field, $\boldsymbol{g}$ is acceleration due to gravity, E_H is a volumetric heating rate due to an unknown coronal heating mechanism, and E_R is the volumetric energy loss rate due to radiation. The thermal conductive flux, $\boldsymbol{F}_C$, is assumed to be given by the Spitzer (1962) formulation

$$\boldsymbol{F}_C = -\kappa_0 T^{5/2} \nabla T, \tag{4}$$

where the coefficient $\kappa_0 \approx 10^{-6}$ in cgs units, and T is temperature in kelvins.

We assume that mass flux and thermal conduction perpendicular to the field are negligible in comparison to their magnitudes parallel to the field. Taking into account this approximation together with the steady state assumption, the force-free assumption ($\boldsymbol{j} \times \boldsymbol{B} = 0$), and magnetic flux conservation, the equations reduce to these four coupled first-order nonlinear differential equations with respect to distance s along the loop:

$$\frac{d\xi}{ds} = 0, \tag{5}$$

$$\frac{dP}{ds} = -\left[\rho g_{\|} + \rho v^2 \left(\frac{d \ln T}{ds} + \frac{d \ln B}{ds}\right)\right]\left(1 - \frac{\rho v^2}{P}\right)^{-1}, \tag{6}$$

$$\frac{dF_c}{ds} = E_H - E_R + v\frac{dP}{ds} + F_c \frac{d \ln B}{ds} - \frac{5}{2} P v \frac{d \ln T}{ds}, \tag{7}$$

$$\frac{dT}{ds} = -\frac{F_C}{\kappa_0 T^{5/2}}.. \tag{8}$$

The variable ξ, defined as

$$\xi \equiv \frac{\rho v}{B}, \tag{9}$$

is equal to a constant times the mass flux, $\rho v A$, where A is the cross-sectional area of the loop. The term ξ is a conserved quantity. The quantity $g_{\|}$ is the parallel component of the acceleration due to gravity,

$$g_{\|} = g_{\rm surf} \frac{dz}{ds}, \tag{10}$$

where $g_{\rm surf}$ is the value of gravity at the solar surface (the photosphere), and z is height above the surface. The E_H and E_R terms are discussed in §§ 2.2.1 and 2.2.2. The ideal gas equation of state completes the set of required relationships,

$$P = \frac{\rho R T}{\mu}, \tag{11}$$

where R is the gas constant and μ is the mean molecular weight per particle (0.5 for a fully ionized pure hydrogen plasma).

Equations (5)–(8) comprise four differential equations for the independent variables ξ, P, F_C, and T. Together with relationships (9)–(11), they represent steady state loops heated by an arbitrary coronal heating mechanism, cooled by radiative losses, and moderated by thermal conduction and enthalpy flux along their axes. The loops have cross-sectional area profiles that vary with the magnitude of the magnetic field strength. They are acted on by gravity and may have steady state flows, with constant mass flux from one footpoint to the other. These flows arise if the heating is asymmetric in the two sides of the loop (e.g., Mariska & Boris 1983; Craig & McClymont 1986). Such asymmetries also arise in loops with uniform volumetric heating but with loop area (field strength) that is asymmetric about the apex.

2.2.1. *The Heating Term*

A choice must be made for the amount of incoming heat energy deposited in loops via a coronal heating mechanism. One application of the modeling technique introduced in this paper is that different choices may be used to predict the emission from different proposed heating mechanisms.

To simulate the appearance of an active region heated by a given coronal heating mechanism, we calculate the heat input based on a parameterized scaling relationship. Mandrini et al. (2000, hereafter MDK00) present how E_H would scale with different quantities such as magnetic field strength, footpoint velocities, etc., for 22 different proposed heating mechanisms in a steady state heating scenario.

We focus on two of these parameters that depend on properties of the magnetic field: field strength, B, and field line loop length, L. We choose to test four different variations of scaling relationships using these two quantities: B/L, B/L^2, B^2/L, and B^2/L^2. These four scaling relationships span a wide range of the heating mechanisms MDK00 present.

We use a length-averaged magnetic field in these parameterizations: $\bar{B} = \int_L |\boldsymbol{B}| ds / \int_L ds$. (For simplicity, we leave off the overbar indicating this average of the B variable when discussing the parameterizations.) An alternative would be a heating rate dependent on the local magnetic field, $E_H \propto B(s)/L$. (Some heating theories from MDK00 predict a heating that scales with the local magnetic field, whereas others depend on the field strength at one location along the loop, such as the footpoint or the location of an instability onset.) However, we find that for typical magnetic field lines in our calculations, the magnetic field drops off very rapidly with height, and our investigations showed that many loops heated in this way did not converge to a steady state solution. Furthermore, as we show in § 6.2, a heating profile that is nearly uniform along the loop length gives results that best match the observations.

The heating scale relationships also require a proportionality constant to determine the total amount of heat deposited. Most commonly, we choose this constant such that the total emission from the model active region equals the total emission of the coronal observations (see § 6.1 for other methods to determine this constant). The relationship between the total emissions and the proportionality constant is typically close to a power law, such that a few iterations swiftly convergence to the correct value.

Using this technique to determine the proportionality constant causes different heating relationships to affect the spatial distribution and morphology of emission throughout the region, but not the total energy radiated (as observed in a given filter).

2.2.2. *The Radiative Loss Term*

The volumetric rate of energy lost due to radiation, assuming an optically thin, fully ionized plasma, is

$$E_R = n^2 \Lambda(T), \tag{12}$$

where $n = n_e = n_{\rm H}$ is the particle density of the plasma, with the electron density n_e equal to the H nuclei density $n_{\rm H}$. This quantity is related to the mass density by: $\rho = n m_{\rm H}$, where $m_{\rm H}$ is the mass of a hydrogen atom. Here, we have assumed that minor species do affect the loss function, $\Lambda(T)$, but we ignore their effects on the equation of state or mass density.

We calculate the radiative loss function using the CHIANTI atomic database, version 4.2 (Dere et al. 1997; Young et al. 2003). Details of this calculation are described in Appendix A.

2.2.3. *Numerical Technique for Loop Solutions*

To calculate loop thermodynamics, we integrate equations (5)–(8) on each side of the loop from footpoint to loop "apex," defined to be the point where the conductive flux reaches zero. (Because of strong gradients in the transition region, the loop equations are very sensitive to small changes in initial values. These cause footpoint-to-footpoint or apex-to-footpoint integrations to be unruly, sometimes yielding oscillating or otherwise unphysical solutions. Footpoint-to-apex integrations are a more conservative, well-behaved choice.) We use a fourth-order Runge-Kutta technique for the integration.

The resolution of the calculation is a function of the temperature gradient. At each location, we set grid spacing equal to the minimum of two quantities: 1/10 of the temperature scale height and 1/100 of the loop length. In addition, grid spacing is halved 10 times near the point where the conductive flux changes sign, to ensure that the location of the loop apex is resolved accurately.

2.2.4. *Boundary Conditions*

Determining appropriate boundary conditions for the independent variables ξ, P, F_C, and T requires some effort. Because the equations are well-behaved only for footpoint-to-apex integrations, boundary values for each variable must be chosen at the base. However, the two legs of the loop must meet at the apex in such a way that thermodynamic variables remain continuous throughout the loop. To achieve this, we vary some of the base values (P and ξ) iteratively until continuity is achieved.

Base values for T and F_C are the only two conditions that can be chosen from a priori physics considerations, rather than iteration. The choice is dependent on the height in the solar atmosphere at which we place the loop footpoint. The footpoint must extend down to temperatures low enough that the neglected portion of the loop (below the model boundary) makes a negligible contribution to both (1) the total radiative cooling of the loop and (2) the radiative emissions produced in the wavelength range of interest. Conversely, the footpoint of the loop must be at a high enough temperature that our assumptions of full ionization and optically thin radiative cooling remain valid. These conditions are met at typical upper chromospheric heights. We choose a chromospheric temperature of $T_{\rm base} = 1 \times 10^4$ K.

Ideally, F_C at the base would be zero (no heat loss through the footpoints; see Rosner et al. 1978), but this results in a singularity in the equations. Instead, we choose an arbitrary value that is tiny enough to be effectively zero as compared to typical values of F_C in the main body of the loop, which range near $\sim -10^7$ ergs cm^{-2} s^{-1} or less in the corona. We take $F_C = -100$ ergs cm^{-2} s^{-1} at the base. The integration continues until the conductive flux returns to zero at the loop apex.

Two more boundary conditions are required from equations (6) and (5): gas pressure, P, at the base and mass flux, ξ. These values cannot be chosen directly, but they are related indirectly to two important pieces of physics that must be incorporated into the loop solutions: (1) loop length, which is a sum of the two separate loop-leg integrations, must equal the total length of the original field line, and (2) all thermodynamic variables of the two legs must match at the apex, to prevent discontinuities. The length of each loop leg is a strong function of $P_{\rm base}$, so consideration (1) is most strongly related to the choice of base pressure. The mass flux, ξ, comes from plasma flows driven by asymmetries in loop heating, as reflected by volumetric asymmetries. Without such a flow, the loop temperature profile would be discontinuous at the apex. Thus, it is consideration (2) that determines the correct value of ξ, a function of the flow velocity.

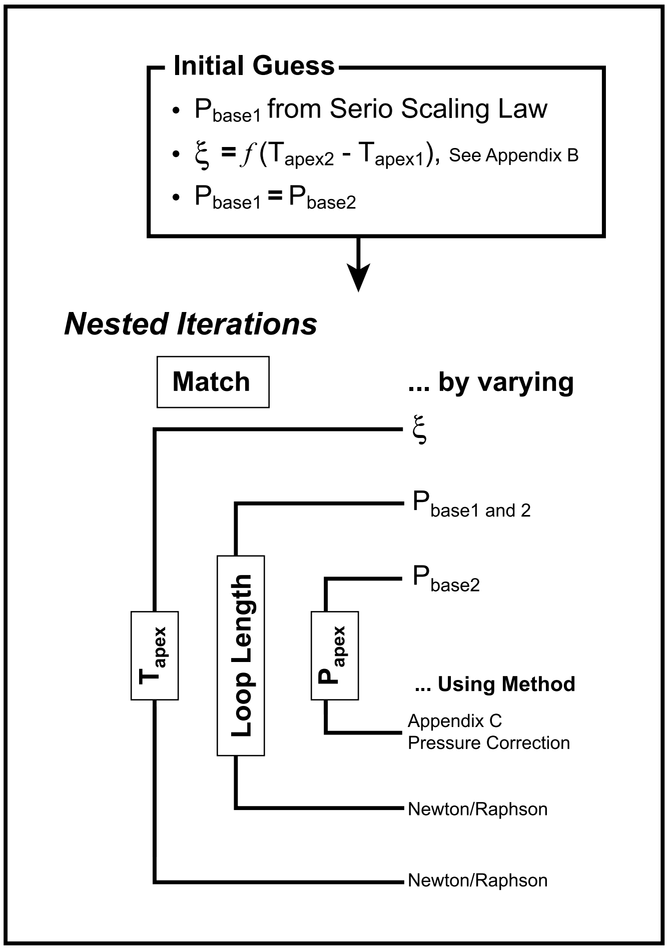

FIG. 1.— Graphical illustration of the nested iterations designed to match both footpoint and apex boundary conditions for each coronal loop calculation. Loop leg apex temperatures are matched by varying the mass flux, ξ. Loop length, L, is matched by varying the base pressure. Loop leg apex pressures are matched by varying the base pressure of the second leg.

We perform a nested sequence of iterations in which we vary the choices of $P_{\rm base}$ and ξ to find the values that meet these physical restrictions. An outline of these nested iterations is given in Figure 1.

Beginning first with a zero-velocity static loop and our best guess for the base pressure (determined from loop scaling laws; as in Serio et al. 1981), we perform a Newton-Raphson iteration to find the base pressure that gives the correct loop length.

If any asymmetric heating between the two legs exists, then the zero-velocity solution will have an apex temperature difference. (Note that any field strength asymmetries result in an asymmetry in cross-sectional area, which, in the case of a uniform volumetric heating term, results in heating asymmetry.) This apex temperature difference can be used to guess the flow from one leg to the other necessary to eliminate the discontinuity (see Appendix B). This guess serves as a starting point for an outer Newton-Raphson velocity iteration to find the proper value for ξ. At each step in this outer iteration, we perform a pressure iteration to ensure that the loop length remains correct. When the nested iteration is complete, loop length matches field line length, and temperature is continuous, both to within one part in 10^4.

Until now, we treated the boundary conditions equally at each footpoint. This is appropriate for T and F_C, since both loops are anchored at the same height in the chromosphere. It is also correct for the mass flux, ξ, which is constant throughout the loop as per equation (5). For P, however, density profile differences or a small plasma flow from one leg to the other effect a slight difference in base pressures of the two legs. Forcing the two base pressures to be equal yields a slight pressure (and density) discontinuity at the apex.

To eliminate this discrepancy, we adjust the base pressure of one loop leg while holding the pressure of the other leg constant during a third iteration (Appendix C). Applying this correction a few times iteratively, within the innermost loops of the nested Newton-Raphson iterations, eliminates the pressure discontinuity sufficiently for most loops. Performing the correction at every step ensures that the velocity iteration will converge to a value consistent with both temperature and pressure continuity. Restricting this correction process to a maximum of five iterations brings most loops (typically 99%) to pressure continuity within 1 part in 10^3. We have chosen to eliminate loops that do not achieve pressure continuity to this degree, a criterion that we find to have a negligible effect on the synthetic emission images.

The first pressure iteration in each nested Newton-Raphson sequence takes about five steps to converge on average. Subsequent pressure iterations (at subsequent steps in the velocity iteration) typically take two to three steps. The velocity iteration that makes up the outermost loop depends strongly on the individual loop magnetic field geometry and profile, and steps required for convergence range from two to about 20. The full code typically takes about 1–2 s to converge per loop on a modern desktop workstation, with about 40 total loop-leg integrations necessary to find a final solution.

In solving loops over an entire active region, we generally find that a small percentage (typically 1%–5%) of loops fail to converge. Of these, some have viable solutions that can be found by hand, but fail to be discovered by one of our convergence algorithms. This is usually due to the presence of a local minimum or to a first guess that is not sufficiently close to the correct solution for convergence. The pressure iteration to determine loop length is particularly sensitive to the initial guess, and our algorithm automatically restarts with a few alternate first guesses if convergence fails. Nevertheless, this approach still fails for some loops with viable solutions. A separate population of loops has no viable solutions. Usually in our applications, these are due to relatively rare pathological behavior, such as the occasional field line whose magnetic field increases with height before decreasing. We eliminate all loops that do not converge, and we assume this to have a negligible effect on emission morphology.

2.3. *Interpolation*

Solving the equations in § 2.2 for each loop yields temperature and density profiles along every closed field line chosen to represent the region. Of course, the field line concept is an artificial one, particularly in a low-β corona where the field is spatially filling. Thus, our synthetic emission images should be relatively insensitive to which field lines are chosen, as long as a representative sample is present. For this reason, we choose to interpolate the temperature and density values from the individual loop solutions to a regular three-dimensional grid. Practical considerations also motivate this step: information on a regular grid enables a quantitative, pixel-by-pixel comparison with the observed emission measure (after integrating over the satellite line of sight).

Finding a suitable three -dimensional interpolation algorithm was one of the more difficult parts of this problem. Well-known methods such as the quickhull (Barber et al. 1996) and Shepherd's methods (Renka 1988a, 1988b, 1988c) resulted in unphysical artifacts near the lower boundary and unstable numerical behavior, respectively. We chose a simple first-order interpolation scheme where the weight of a loop solution "data point" depends on the volume of the portion of cell between it and the grid point, and on the length of the line segment connecting adjacent loop solution points. The loop solution data points to be interpolated onto the uniform grid are themselves linearly interpolated to the midpoints of the line segments connecting adjacent points in the loop solutions. Our scheme for the value f assigned to a gridpoint at $\boldsymbol{x_i}$ from coronal loop data points at $\boldsymbol{x}_1, \boldsymbol{x}_2, \ldots \boldsymbol{x_n}$ is

$$f(\boldsymbol{x_i}) = \frac{\sum_n W_i(\boldsymbol{x_n}) f(\boldsymbol{x_n})}{\sum_n W_i(\boldsymbol{x_n})}, \tag{13}$$

where $W_i(\boldsymbol{x_n})$ is the weight toward the ith grid point from the nth data point. For an equally spaced grid with unit cell size, this weight is defined as

$$W_i(\boldsymbol{x_n}) \equiv \begin{cases} (1 - |x_n - x_i| \times |y_n - y_i| & \text{for } x_{i-1} < x_n < x_{i+1}, \\ \quad \times |z_n - z_i|)\Delta s_n, & y_{i-1} < y_n < y_{i+1}, \text{ and} \\ & z_{i-1} < z_n < z_{i+1}, \\ 0, & \text{otherwise,} \end{cases} \tag{14}$$

where x, y, and z represent the three Cartesian components of a position vector $\boldsymbol{x}$. The quantity Δs_n is the length of the line segment connecting two adjacent loop solution points. Including the Δs_n factor in the weighting function ensures that solution points representing small volumes within the grid cell are given less weight than those representing larger volumes.

This first-order method relies only on nearest neighbor points to determine interpolated gridpoint values, preventing excessive smoothing and ensuring that the predicted emission measure is affected by only nearby plasma, not more distant field lines. It results in a computed value of zero if there are no field line data points near the grid voxel. The accuracy of this interpolation scheme is discussed in § 3.4.

2.4. *Synthetic Images*

The interpolation process yields temperature and density values at every point in a three-dimensional data cube representing the active region. We now wish to create the image that a coronal observing instrument would see if it observed an active region with these temperature and density values.

The first few steps of this process actually occur prior to the interpolation step. First we must spatially co-align the photospheric magnetogram data with data from the coronal imager, a surprisingly involved procedure. We begin by co-aligning white light continuum data from our vector magnetogram instrument with equivalent data from the Michelson Doppler Imager (MDI) onboard the *Solar and Heliospheric Observatory* (*SOHO*) mission. This is necessary due to the relatively poor pointing information from Earth-based vector magnetogram instruments, such as the Imaging Vector Magnetograph (IVM) used in our example. The IVM pointing data can be off by as much as 100″ (Leka & Barnes 2007).

MDI provides a bridge between the magnetogram instrument and the coronal EUV/X-ray instrument in that (1) it has full-Sun measurements which allows for co-alignment with coronal imaging data based on the easily distinguished edge of the solar disk, and (2) it has white light continuum data which allow for feature-based co-alignment with analogous data from magnetograph instruments. (Note that MDI also has line-of-sight magnetogram data that could be used for co-alignment with magnetograph data, but we find that the continuum data yield better results.) We employ a polynomial warping algorithm (`poly_2d` in IDL) to co-align the white light features (primarily sunspots).

After MDI co-alignment, we transform the data into heliographic (disk center) coordinates, a step required for most coronal magnetic field extrapolation algorithms. For a detailed description of this transformation see Gary & Hagyard (1990). We perform the coronal magnetic field extrapolation, field line integration, and loop energy calculations in the heliographic coordinate system. To reconstruct a synthetic emission image, we transform these data back to image coordinates of the imaging satellite prior to interpolation.

For interpolation, we choose a three-dimensional grid with a z-axis parallel to the line of sight of the satellite (normal to the instrument image plane). The x and y gridpoints are chosen to lie at pixel centers of the observed coronal images.

We use the temperature and density values interpolated to the three-dimensional grid to calculate emissions at each grid voxel. We first calculate an intensity spectrum using CHIANTI. With information about the instrument response and the effective area as a function of wavelength for the filter used to observe the active region, we can calculate the expected number of CCD electrons recorded by the imaging instrument due to photons emitted from each grid voxel (see Appendix A). We integrate these emissions over the satellite line of sight (the z-axis of our interpolation grid) to produce a quantitative prediction of the number of CCD electrons recorded for each pixel of the active region observation, a synthetic emission image.

One disadvantage of performing simulations in heliographic coordinates is that our simulation volume, which is normal to the Sun, does not fully overlap with the volume that contributes to the final projected two-dimensional image, which is normal to the image plane (unless the observed image lies exactly at disk center). For images away from disk center, the satellite line-of-sight integration will at some locations pierce only a small corner of the simulation box. The predicted emissions at these points do not reflect emissions from the full height of the corona.

3. RESULTS

In §§ 3.1–3.4, we present results for the modeling of NOAA-designated Active Region 8210 (AR 8210), observed on 1998 May 1.

3.1. *Magnetogram Data*

Photospheric vector magnetogram data for AR 8210 are available from the IVM instrument at University of Hawaii's Mees Solar Observatory on Haleakala (Mickey et al. 1996; LaBonte et al. 1999). We choose data from 1998 May 1 at 19:42 UT. The resolution of the 180° ambiguity in the component transverse to the line of sight was performed using the method of Canfield et al. (1993) followed by a minimization of the divergence of $\boldsymbol{B}$ and of the vertical currents J_z. Figure 2 shows the reduced data.

3.2. *Magnetic Field Solution*

To compute the quasi–force-free coronal magnetic extrapolation (§ 2.1.1) from the vector magnetogram of Figure 2, we transform the data to heliographic coordinates and rebin it to 128×128 pixels, to reduce the calculation time. In this case, the $128 \times 128 \times 128$ three-dimensional solution took about 14 hr to run on a desktop workstation.

Figure 3*a* shows all the field lines from our coronal extrapolation. Note that the magnetogram edge is not parallel to the fff

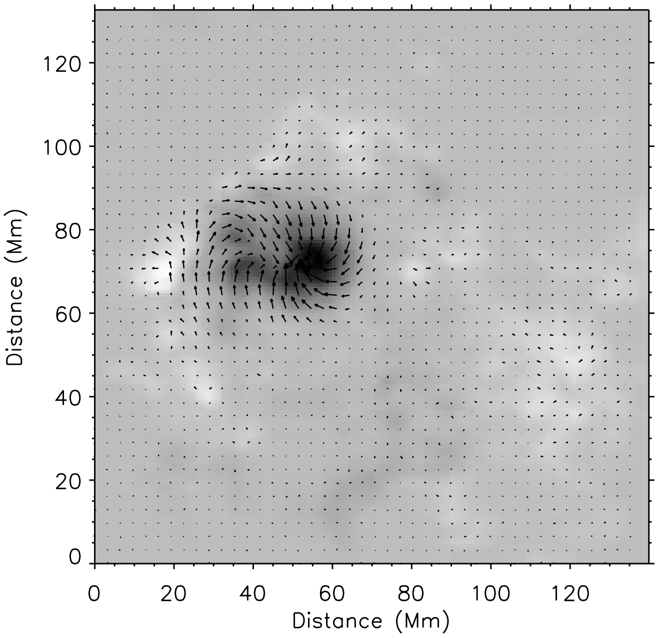

Fig. 2.—Vector magnetogram of Active Region 8210 on 1998 May 1, 19:42 UT, rotated to disk center from latitude −0.22 rad, 0.10 rad from central meridian, with a solar *B*-angle of −0.07 rad and a solar *P*-angle of −0.42 rad. Gray scale indicates the strength and direction of the *z*-component of the magnetic field (i.e., the vertical component after the rotation is completed), with white as positive polarity and black as negative. Maximum vertical field is about 1150 G; minimum is −3320 G. Arrows show the tangential magnetic field, with maximum arrow length indicating a strength of 2380 G. [*See the electronic edition of the Supplement for a color version of this figure.*]

boundary box in heliographic coordinates. For this region, which has a maximum magnetic field strength greater than 3300 Gauss, we draw a field line from every pixel on the bottom boundary at which the field strength is 50 Gauss or larger. Of the 16,384 pixels on the bottom boundary, 5057 of them have a value above this threshold and generate a field line. Of these lines, 727 are “open,” by our definition of the term, i.e., they close on the edge of the box of extrapolated field. Another 155 of them are too short to yield meaningful results in our loop solutions (fewer than 3 points long, with point spacing determined by the resolution of the field extrapolation). Thus we are left with 4175 closed field lines, which are shown in Figure 3*b*. These represent the loops along which we solve the loop equations.

The extrapolation technique involves a minimization of the field divergence, and we find that the solution is relatively divergence-free. The best measure of this is to use a normalized divergence, dividing the divergence, $\nabla \cdot \boldsymbol{B}$, by $(B/\Delta z)$, the magnetic field divided by the typical grid spacing, to get a dimensionless quantity. Since we care most about the divergence in regions of large magnetic field, we take a field-strength weighted average of this quantity, and find it to be relatively small,

$$\frac{\sum_i B_i\left(|\nabla \cdot \boldsymbol{B}|_i \Delta z_i / B_i\right)}{\sum_i B_i} \simeq 0.02. \qquad (15)$$

3.3. *Loop Calculation Results*

We calculate temperature and density along each of the field lines in Figure 3. Figure 4 shows different terms in the energy equation (7) for a sample coronal loop calculation from this region. The code conserves energy very well, even in the presence of the strong gradients that characterize the transition region. Figure 5 shows temperature, pressure, particle density, and magnetic field for the same line.

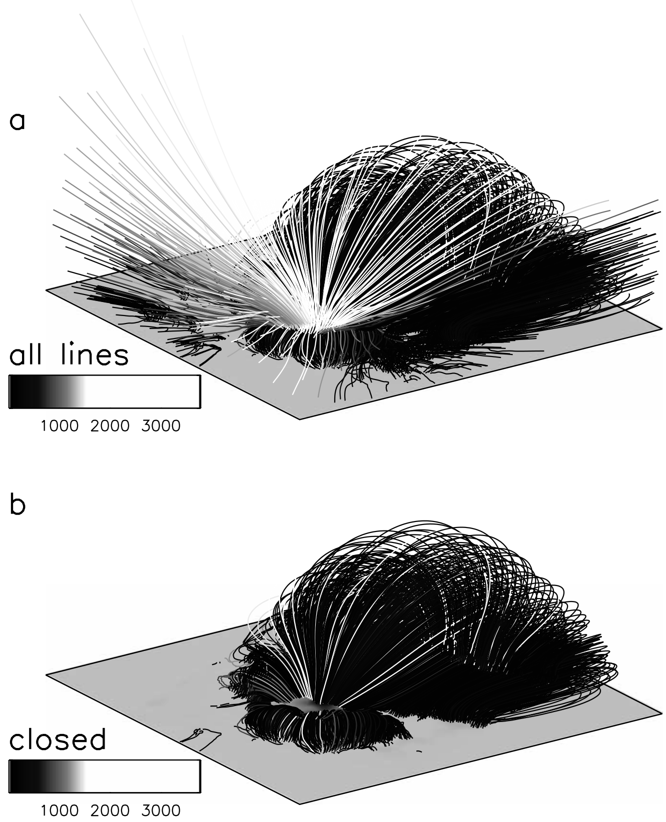

Fig. 3.—(*a*) Side view of all of the field lines from the coronal field extrapolation of AR 8210. Gray scale at the bottom boundary shows vertical magnetic field. Field line color scale shows base magnetic field strength (on a strongly saturated color scale). (*b*) Same view, with field lines removed that are too short to use or “open.” [*See the electronic edition of the Supplement for a color version of this figure.*]

Figure 6*a* shows a comparison with the analytic solution of Rosner et al. (1978). The analytic solution requires static loops (no flows), no gravity, no area variations, and a power law approximation for

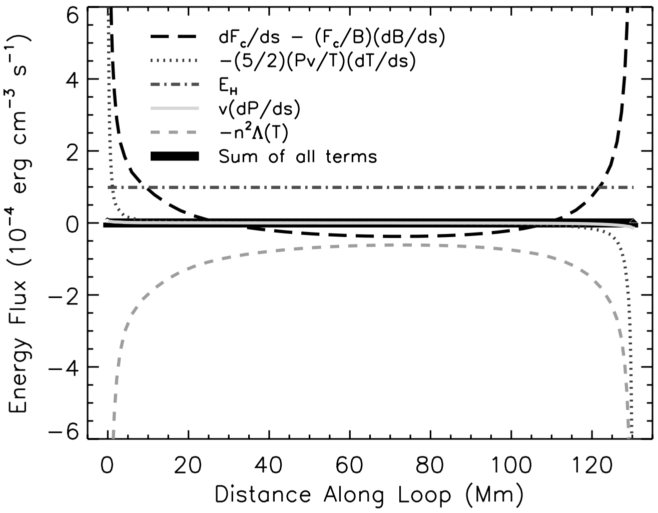

Fig. 4.—Terms from the energy equation (eq. [7]) for a sample loop calculation from AR 8210. Energy is very well conserved even in the presence of strong gradients of the transition region. [*See the electronic edition of the Supplement for a color version of this figure.*]

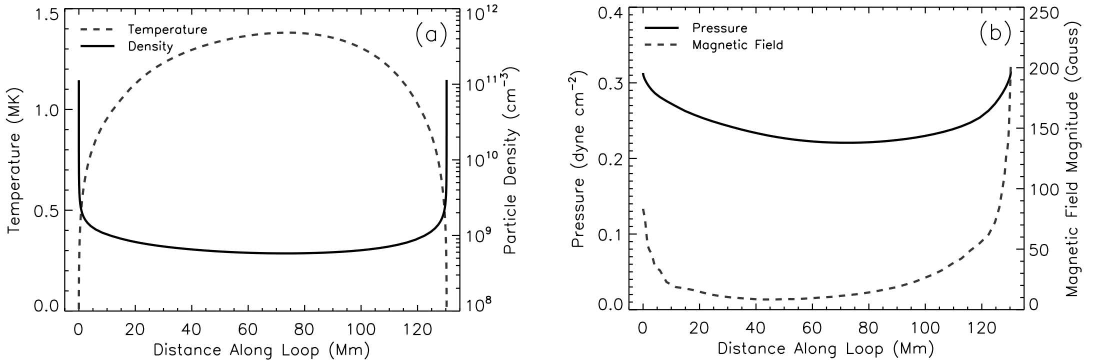

FIG. 5.—(*a*) Temperature and particle density for a sample loop calculation from AR 8210. (*b*) Pressure and magnetic field strength from the same loop. [*See the electronic edition of the Supplement for a color version of this figure*.]

the radiative losses, so for comparison we show a version of our numerical code that matches these assumptions.

Figure 6*b* shows the effect of the features ignored in Figure 6*a*. The bottom loop shows results using the Rosner et al. (1978) assumptions. The next curves represent loops with additional features from our code added on in succession: gravity, a radiative loss function calculated using the CHIANTI atomic database, cross-sectional area variations that vary with loop magnetic field strength, and finally, plasma velocity flows. Note that the loop with area variations and no flows has a discontinuous temperature profile at the apex, showing the necessity of steady state flow to achieve a reasonable equilibrium solution.

Using the simulation of AR 8210 with B/L heating as an example, we find that of the 4175 closed coronal loops, 65 were unable to converge to a steady state solution. An additional nine were unable to achieve sufficient pressure continuity under the conditions established in § 2.2. These loops, representing 1.8% of the total, are discarded, and we use the remaining 4101 loops to build the predicted emission image for the active region.

3.4. *Interpolation Results*

One measure of the accuracy of our interpolation scheme is to compare the interpolated magnetic field values to the original magnetic field values. The original three-dimensional, extrapolated coronal field is calculated on a $128 \times 128 \times 128$ grid. From this volume, field lines are calculated using the method described in § 2.1.2, and magnetic field values are interpolated onto these lines using a standard three-dimensional bicubic calculation with a $\nabla \cdot \boldsymbol{B} = 0$ condition applied. After these field lines are used for the energy calculations, the thermodynamic values are interpolated back to a regular grid using the first-order formulation described in § 2.3.

We tested the interpolation accuracy by using this same method to interpolate the magnetic field strength values from the field lines back onto the original regular grid. Because we have purposely employed a first-order scheme where the gridpoints far from field lines are set to zero, we consider only the nonzero interpolated gridpoints in measuring the accuracy of the method. Of these nonzero points, we take a field-weighted average of the fractional difference between the interpolated and original values,

$$\frac{\sum_i B_i * (|\Delta B_i|/B_i)}{\sum_i B_i} \simeq 0.039, \qquad (16)$$

where ΔB is the difference between the interpolated and original B values. We find that we are typically off by about 4%, which compares favorably to other interpolation schemes we tested.

It is important to recall that this measurement ignores the undersampled areas where the interpolated field is zero. In reality, the magnetic field is relatively continuous in the low-β, field-filling corona. In contrast, observations suggest that thermodynamic variables are not very continuous, as evidenced by the appearance of individual coronal loops that stand out from the background for reasons that remain unclear. The first-order scheme we developed in this paper has similar behavior and seems to produce fewer artifacts in the thermodynamic variables and the

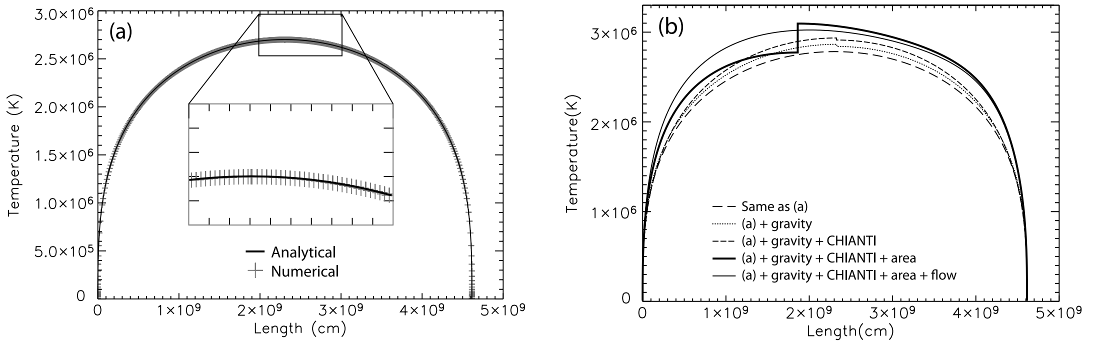

FIG. 6.—(*a*) Comparison of analytic solution from Rosner et al. (1978) with our numerical results, using the assumptions of Rosner et al.: no gravity, radiative losses approximated with a power law, area variations removed (i.e., magnetic field taken to be uniform, with a value equal to the average of the original field line), and zero plasma flow velocity. (*b*) Effect of progressively adding in features of our code, as compared to the analytical solution (*long-dashed line*): gravity (*dotted line*), both gravity and a radiative loss function calculated using CHIANTI (*short-dashed line*), and these features plus cross-sectional area variations due to the change in magnetic field along the field line (*thick solid line*). Thin solid line shows final version calculated by our code, with all of the preceding characteristics, plus a steady state flow caused by heating asymmetries.

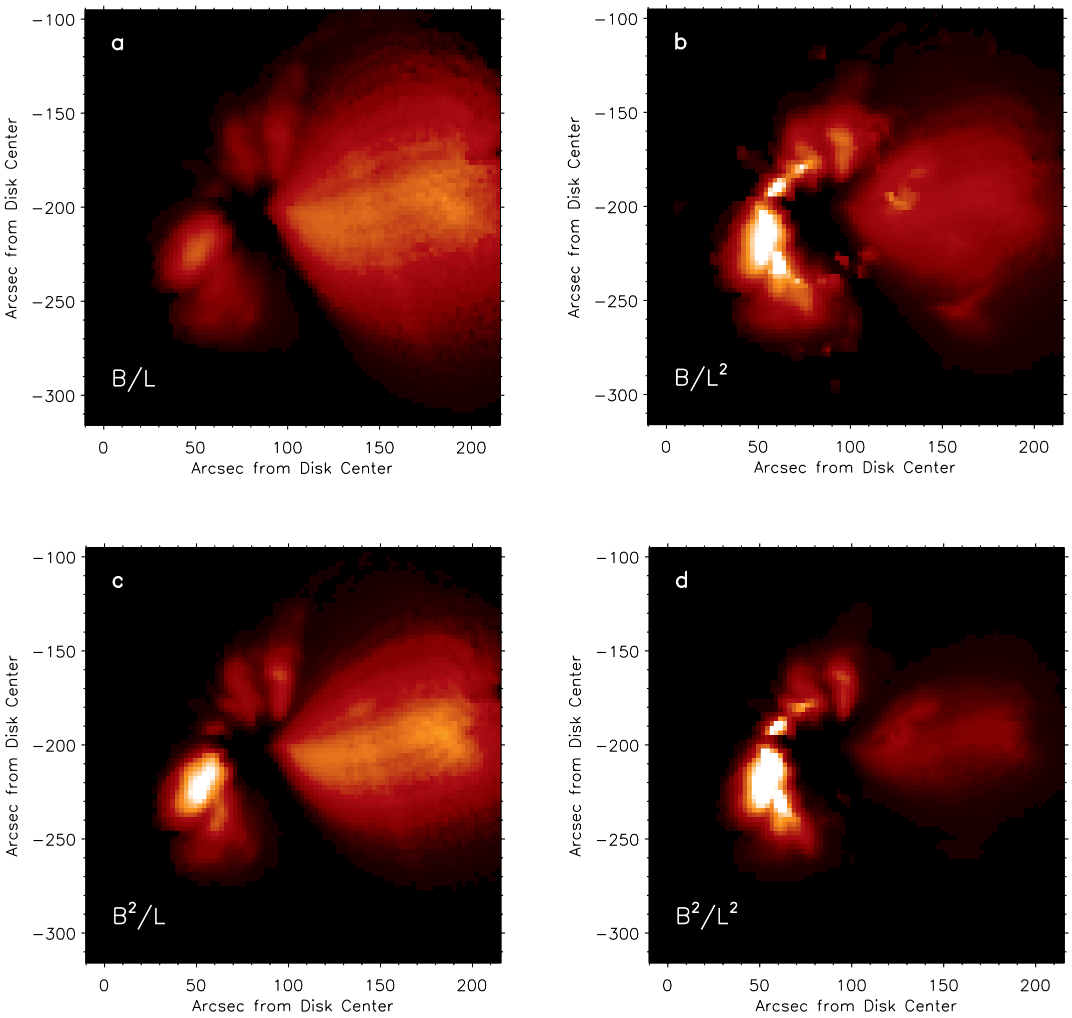

Fig. 7.—Four synthetic SXT images of AR 8210, created with these different scaling relationships for the heat energy flux: (*a*) B/L, (*b*) B/L^2, (*c*) B^2/L, and (*d*) B^2/L^2. These images are synthesized from magnetogram data taken at time 19:42 UT. All panels use same color scale.

resulting emissivity than the other interpolation techniques we explored.

4. COMPARISON WITH OBSERVATIONS

Figure 7 shows synthetic images of AR 8210, made using four different heating parameterizations described in § 2.2.1. These images were created to simulate observations from *Yohkoh* SXT, using the Dagwood sandwich filter (AlMgMn). We used an exposure time of 339 ms (to match observations available at the time of the magnetogram).

We show the synthetic image enclosed within the smallest rectangle that encompasses all of the field lines that were modeled. However, some locations, such as the black area on the left side of the image, have only a very small number of field lines that meet our criteria (base field strength 50 Gauss). Thus, these regions have little or no visible emission.

Figure 8 shows the observations to which we compare these predictions. The synthetic images in Figure 7 are interpolated to the resolution of the SXT observations, which in this instance is 2.46″ pixel^{-1}. Qualitative and quantitative comparisons are discussed in §§ 4.1 and 4.2.

4.1. *Qualitative Comparison*

Here we discuss how well different heating parameterizations predict the general pattern of observed coronal emissions. The

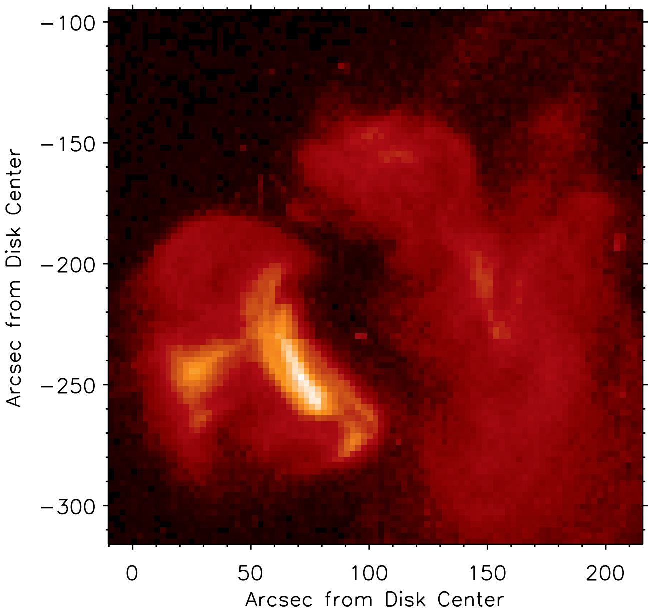

Fig. 8.—*Yohkoh* SXT observations of AR 8210, taken in two parts with the AlMgMn filter at 19:39:41 UT (*bottom half*) and 19:39:57 UT (*top half*) on 1998 May 1.

TABLE 1

AR 8210 Comparison with Observations

Scaling	C	r	s	σ	$\log(T)$	$\log(\mathrm{EM})$
B/L	8.3×10^4	0.11	0.52	2.3	6.48	48.71
B/L^2	4.7×10^{14}	0.34	0.61	2.8	6.40	48.97
B^2/L	3.5×10^2	0.25	0.54	2.1	6.48	48.74
B^2/L^2	1.1×10^{12}	0.26	0.59	4.1	6.44	48.83
Observed	. . .	1	1	0	6.60	48.30

Notes.—Comparison table includes Pearson correlation coefficient, r, Spearman rank correlation coefficient, s, intensity-weighted rms relative error, σ, and log of single temperature and emission measure values, T and EM, respectively. Comparison values are all relative to observations. For predictions identical to observations, $r = 1$, $s = 1$, $\sigma = 0$. The term C denotes the proportionality constant in heating function, as described in § 2.2.1. The units of C vary, but are always such that C times the scaling relationship is equal to the volumetric heat flux in units of ergs cm^{-3} s^{-1}. The T values are expressed in kelvins, and EM values are expressed in cm^{-3}.

observations appear to have three primary "lobes" of bright emission: a large set of loops covering most of the left half of the image, a small lobe situated near the top center of the image, and a long oblong oval-shaped block of emission on the right. In between the large lobes on the left and right is a long, extended dark cavity, situated over the sunspot associated with this active region, as is commonly observed (e.g., Pallavicini et al. 1979; Webb & Zirin 1981; Golub et al. 1990, 1994; Harmon et al. 1993; Vourlidas et al. 1997; Nindos et al. 2000). Some of the synthetic images, particularly B/L and B^2/L, also have three lobes of emission in roughly the same locations, although the size, shape, and spatial extent of the lobes is not well represented.

From comparison with Figure 3, the left lobe of emission is mostly associated with an arcade of small, low-lying loops (located in the front bottom corner of the figure), while the lobe of emission on the right side of the image is characterized by a set of mostly large loops, as well as some small, underlying loops. The dramatic differences between the panels in Figure 7 demonstrate that these two types of field structures emit very differently with different coronal heating functions. In this example, ignoring the morphological shape of the lobes of emission, it appears that the B/L form for the heating overestimates the emission from weak, long loops and underestimates emission from strong, short loops. In contrast, the B^2/L^2 form of heating mechanism appears to have the opposite problem.

The dark lane in the center of the observations is visible to varying degrees in each of the four synthetic images. In the synthetic images, this lane is due to the very long field lines with lower emission, as well as open field lines (or lines which close outside our model box), which are excluded from the calculation, but are likely to contribute little to the overall emission. This area is likely associated with a separatrix region or quasi separatrix layer directly above the sunspot, given that field lines on either side of the dark lane close in opposite directions.

4.2. *Quantitative Comparisons*

Numerous options exist for quantitatively comparing the synthetic images (Fig. 7) with the observations (Fig. 8). We discuss several of these options and their pitfalls here: (1) a correlation coefficient between the pixels in the observation image and the synthetic image, (2) a rank correlation coefficient, (3) intensity distribution comparisons, (4) an intensity-weighted rms relative error, and (5) a comparison of single filter-ratio average temperature and emission measure values in the two images.

4.2.1. *Pixel-by-Pixel Correlation*

One way to compare images is to calculate a correlation coefficient, r, between the two images. This quantity (also known as the product-moment correlation coefficient or Pearson's r) is defined as follows. For two sets of pixels, an observed set $\{o_i\}$, $i = 1, \ldots, N$, and a predicted set $\{p_i\}$, we have

$$r = \frac{\sum_i (o_i - \bar{o})(p_i - \bar{p})}{\sqrt{\sum_i (o_i - \bar{o})^2}\sqrt{\sum_i (p_i - \bar{p})^2}}, \tag{17}$$

where $\bar{o}$ and $\bar{p}$ indicate mean values of the sets $\{o_i\}$ and $\{p_i\}$. For the images shown in Figure 7, the correlation coefficients are shown in Table 1. Figure 9a shows a scatter plot with a pixel-by-pixel comparison of intensities for the B^2/L case. The correlation coefficient quantifies how well a linear trend line can fit the data in this plot.

4.2.2. *Rank Correlation*

The rank correlation (Spearman's rank coefficient s) of two images is calculated by ranking the pixels in order of brightness

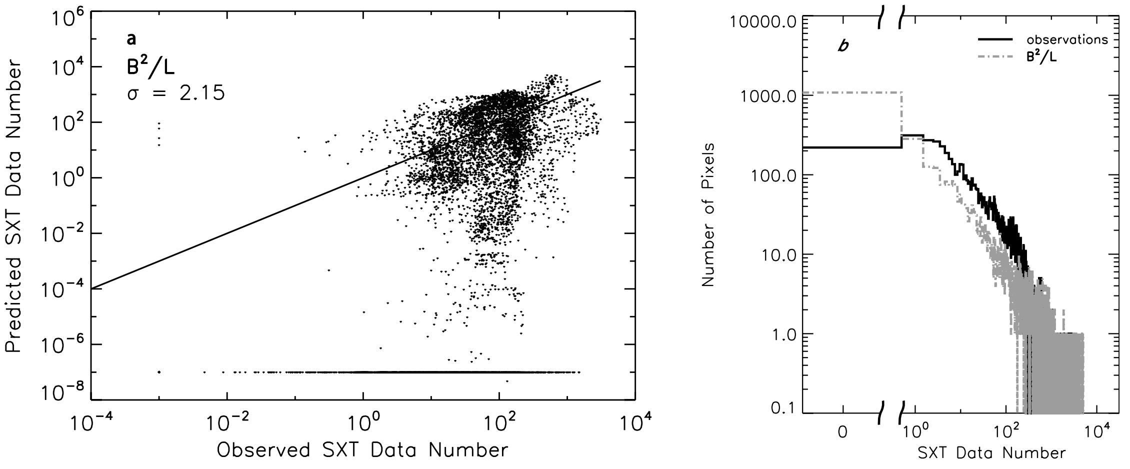

Fig. 9.—(a) Scatter plots showing pixel intensities of the observations vs. the predicted images for B/L^2 heating. Solid line indicates $y = x$, the line on which all the points would be situated if the predictions were exactly right. (Note this is not the same as the best-fit trend line of the points.) Zero values were set to 10^{-3} in the observations and 10^{-7} in the synthetic images to force their appearance on a log-log plot. (b) Histrogram showing pixel intensity distributions for the observations vs. synthetic images for B^2/L heating. [*See the electronic edition of the Supplement for a color version of this figure.*]

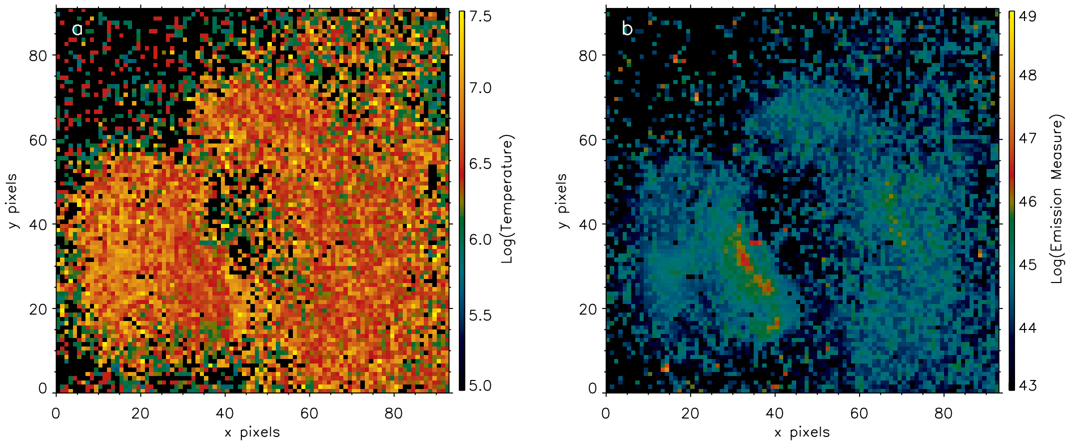

Fig. 10.—(*a*) Temperature and (*b*) emission measure values for AR 8210 derived from Dagwood sandwich (AlMgMn) and thin aluminum (Al.1) filter ratio.

and then calculating the correlation between the rank values. The method eliminates consideration of absolute intensities and only compares whether bright areas in one image are located in the same place as bright areas in the other image. Rank correlations between the synthetic images and observations are given in Table 1.

The rank correlation test also enables an explicit significance test, because the distribution of the ranks is always a known function. In all of the four cases listed in Table 1, the significance of the correlation is better than machine precision, i.e., there is less than 1 chance in 10^{45} that the observed correlation would result from a random distribution.

4.2.3. *Intensity Distributions*

The correlation tests indicate whether pixels in the observations and predictions are correlated, but say nothing about the similarity of the point distributions between the images. In fact, we find in this case that the image with the lowest correlation coefficient, B/L, has a pixel intensity distribution function most similar to the observations.

The distribution of intensities for the B/L synthetic image is quite similar to the observed distribution. The largest discrepancy occurs in the B^2/L^2 case. This case contains many outliers, some a full order of magnitude or more larger than the maximum emission in the observations. Because the total emission in every case is the same by construction, these outliers are necessary to balance out the larger number of pixels with low emission. Figure 7 shows that the bulk of the emission emanates from these outliers, situated in the left lobe of the image. The distribution also indicates that the B^2/L^2 heating predicts too much contrast between low-emission and high-emission regions. Many pixels are in the bottom bin with smallest emissions, but the high-emission tail of the distribution is also large. Few pixels lie between the extremes. Figure 9*b* shows an example of the intensity distribution for the B^2/L case.

4.2.4. *Weighted rms Relative Error*

The correlation coefficient is essentially a measure of the scatter from the best-fit line, of any slope, that could be drawn through points in a scatter diagram such as the ones in Figure 9*a*. What we really want is a measure of the deviation from a line with slope 1, $y = x$, because ideally we want to reproduce the image exactly. One measure of this would be the rms deviation from that line. Even better would be some measure of the normalized deviation, rather than the absolute deviation. We normalize the deviation by the intensity of each pixel in the observed image to get a relative error.

However, taking the rms of this relative error is misleading, because it is heavily influenced by small deviations from very low intensity pixels. For example, pixels that predict zero intensity where there is only a very tiny intensity actually observed will still have a relative error of 100%. There are a number of pixels of this type, given that our method systematically underestimates the low-intensity background emission due to open field lines (or long field lines that close outside the box) not represented in our calculation. To mitigate this problem, we use an intensity-weighted mean in the rms calculation, rather than a straight mean. We call this an intensity-weighted rms relative error, σ, defined as follows for the observed pixels $\{o_i\}$ and predicted pixels $\{p_i\}$:

$$\sigma = \sqrt{\frac{\sum_i o_i[(o_i - p_i)/o_i)]^2}{\sum_i o_i}}. \tag{18}$$

This value gives a measure of the typical relative error of predicted versus observed pixel intensities. The results are shown in Table 1. Our best prediction, given by a scaling that goes as B^2/L according to this estimate, is typically about 210% off. This illustrates that all of the proposed heating parameterizations under investigation do a poor job of predicting the observed emission pattern in this active region.

4.2.5. *Temperature and Emission Measure Comparisons*

Another important measure of forward modeling accuracy is to compare temperature and emission measure values between the predicted and observed active regions. The observed temperature and emission measure values at each pixel, as inferred from a simple filter ratio inversion are shown in Figure 10, while plots of the same values for each of the synthetic images are given in Figures 11 and 12. In all cases, the results are calculated with the `sxt_teem` function in SolarSoft (Freeland & Handy 1998), using the AlMg and Al1.1 filters, with the filter ratio calculated using response functions from Appendix A.

For the predicted values, synthetic images were created for the two different filters, using the same proportionality constant. The constant was chosen to match the total emission in the AlMg filter. We note that the filter ratio technique is unreliable in regions where there is little emission, causing the low-intensity data points in Figure 10 to be quite noisy.

To compare the images in Figures 10, 11, and 12, we could employ the diagnostics developed in § 4.2.4 for synthetic images, but our observed temperature and emission measure values

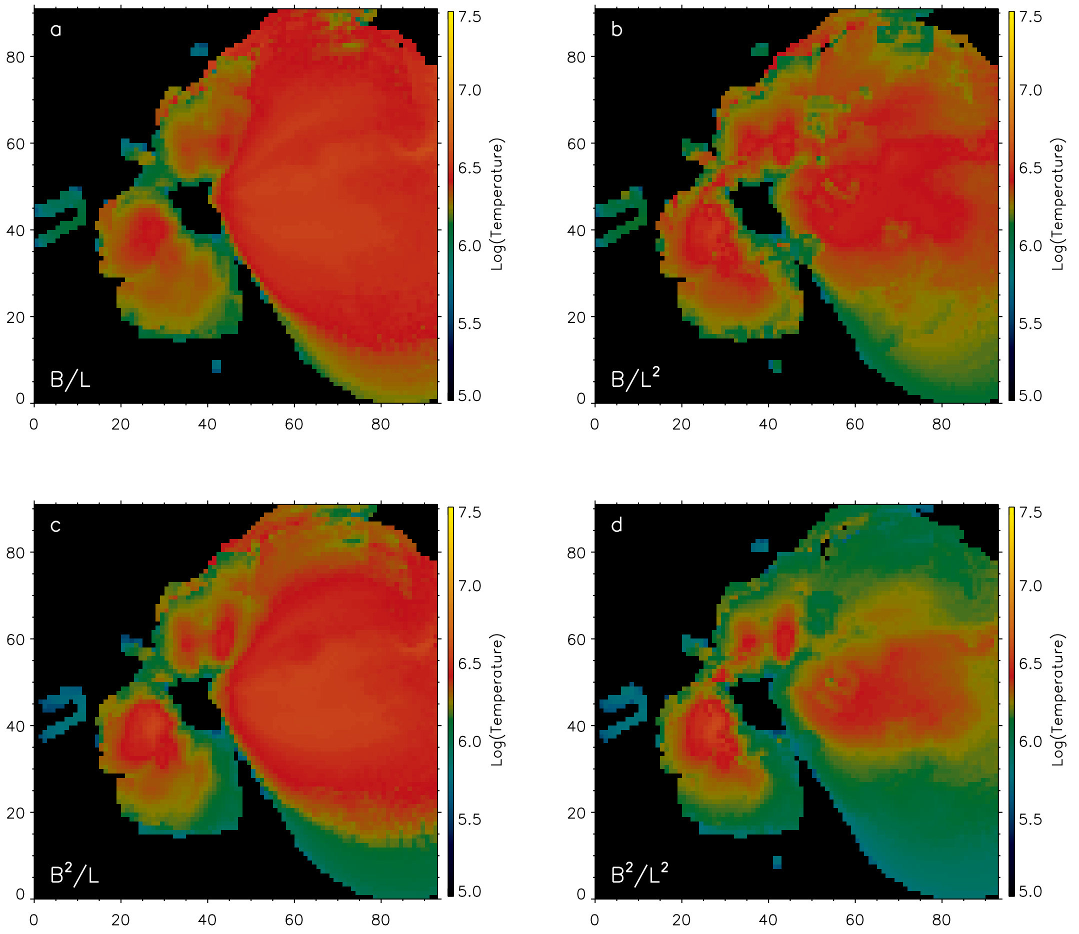

FIG. 11.—Filter ratio temperature values for synthetic images predicted for heating relationships (*a*) B/L, (*b*) B/L^2, (*c*) B^2/L, and (*d*) B^2/L^2. Color scale is same as Fig. 10*a*.

turn out to be too noisy for those comparisons to be very meaningful. A better option is to calculate "single" temperature emission measure values by summing the emission across all pixels in two images based on different observational filters. We calculate one temperature and one emission measure value for the whole region from the ratio of these sums. The results are given in Table 1.

These single-filter-ratio values effectively represent a brightness-weighted average of temperature and emission measure. Because our simulations also calculate temperature throughout the model volume, it is instructive to compare the filter ratio–derived temperature with a simple mean of the interpolated temperature values from the simulation grid. Table 2 gives the results, as well as a similar calculation comparing the single-filter-ratio emission measure to an analogous average quantity, $\bar{n}^2 V$, with $\bar{n}$ as the mean particle density and V as the volume. The comparison gives some feel for the effect of the brightness-weighted averaging of the filter-ratio technique. Note that our averages in these calculations exclude the undersampled pixels assigned to zero by our interpolation scheme.

5. SENSITIVITY TO MAGNETIC FIELD DIFFERENCES

In this section, we investigate how sensitive our predicted SXT emissions are to the coronal magnetic field solution. We look at two issues: the method of solving for the coronal magnetic field (§ 5.1) and the method of representing that solution using discrete field lines (§ 5.2). For simplicity, we present synthetic images only from the B/L scaling relationship for heating.

5.1. *Field Extrapolation Method*

For the images in Figure 7, we computed the coronal magnetic field using the nonlinear quasi–force-free field method described in § 2.1.1. Here, we compare the results to a potential field extrapolation, using only the radial magnetic field data at the photosphere as input. We have employed the Green's function method of Sakurai (1982) for the potential field solution, which avoids the assumption of periodic boundary conditions inherent in other methods. Figure 13 shows the field line representation and the synthetic image generated from this solution in comparison with the quasi–force-free model. Table 3 shows how calculating the field differently changes the quantitative comparison with the observations.

In this case, the improvement of the force free field solution over the potential field extrapolation is small enough to be negligible. This is true even though the active region has transverse field components at the photosphere that are clearly nonpotential, with significantly nonzero mean α and distribution of α, and has a history of flaring, both before and after the time shown in this example, so we would not expect its magnetic field to be potential.

5.2. *Field Line Representation*

In addition to changing the technique for determining the coronal magnetic field, we can also change the field lines with which we represent a given coronal field solution. The field line representation is an artificial one, so we want to be sure that we are using enough field lines to adequately represent the spatially filling

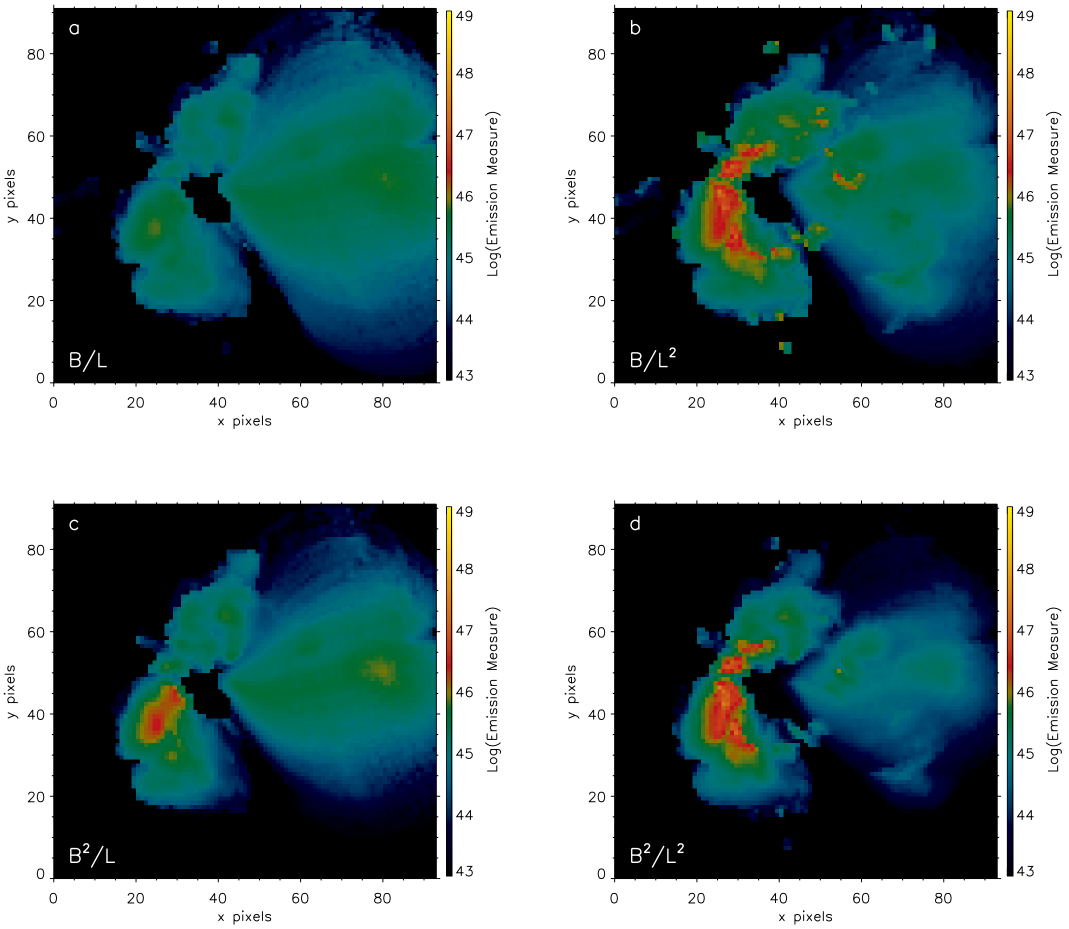

FIG. 12.—Filter ratio emission measure values for the synthetic images predicted for heating relationships (*a*) B/L, (*b*) B/L^2, (*c*) B^2/L, and (*d*) B^2/L^2. Color scale is same as Fig. 10*b*.

magnetic field. This is accomplished by choosing a lower threshold value (1 G) for a pixel from which we choose to draw a field line. The synthetic emission image created from this set of field lines and diagnostic statistics (Table 3) are essentially identical to our reference case. Thus we have chosen an adequate number of field lines to represent the region with our original 50 G cutoff.

We also examine the effects of choosing a different algorithm for drawing field lines. In all previous cases, field lines were drawn starting from every pixel on the bottom boundary having a magnetic field strength above a given threshold value. However, this leaves some low field-strength regions with no data whatsoever. Here we try distributing field lines equally spaced along the bottom boundary. In this case, we have drawn field lines from half of the pixels, skipping every other pixel. The diagnostics in Table 3 show that this, too, makes little difference to the resulting synthetic emission.

Overall, we find that the synthetic images are relatively insensitive to several different magnetic field representation options. This does not necessarily mean that the primary sources of error are due to something other than the magnetic field, but if the magnetic field representation is a large source of error, then fixing it will not be straightforward.

TABLE 2
TEMPERATURE AND EMISSION MEASURE COMPARISON

Scaling	$\log(\bar{T})$	$\log(T_{\rm FR})$	$\log(\bar{n}^2 V)$	$\log(\mathrm{EM}_{\rm FR})$
B/L	6.40	6.48	45.71	48.71
B/L^2	6.32	6.40	45.62	48.97
B^2/L	6.34	6.48	45.57	48.74
B^2/L^2	6.19	6.44	45.22	48.83
Observed	...	6.60	...	48.30

NOTES.—This table compares mean of temperature throughout model volume, $\bar{T}$, with temperatures from single filter ratio technique, $T_{\rm FR}$. These may be compared with the observed single filter ratio value of 6.60. Likewise, we compare the product of the square of the mean density, $\bar{n}^2$, and the volume, V, with emission measures calculated from single filter ratio value, $\mathrm{EM}_{\rm FR}$. These may be compared with observed single filter ratio value of 48.30. Mean values are calculated using only nonzero-valued points in the three-dimensional interpolated grid. The T values are expressed in kelvins, and EM values are expressed in cm^{-3}.

6. SENSITIVITY TO LOOP MODELING DIFFERENCES

In this section, we investigate how several assumptions inherent in our loop model might affect predicted SXT emissions. We consider the effects of a filling factor (§ 6.1), the distribution of coronal heating within loops (§ 6.2), and different assumptions for iron abundances in the corona (§ 6.3).

6.1. *Filling Factor*

Table 1 shows that all of our different heating parameterizations overestimate the emission measure and underestimate the temperature of this active region. The emission measure is off by a factor of about 1.5 even for the best-case scenario. We can remove this discrepancy by invoking a "volumetric filling factor" representing the fraction of coronal volume that is filled with

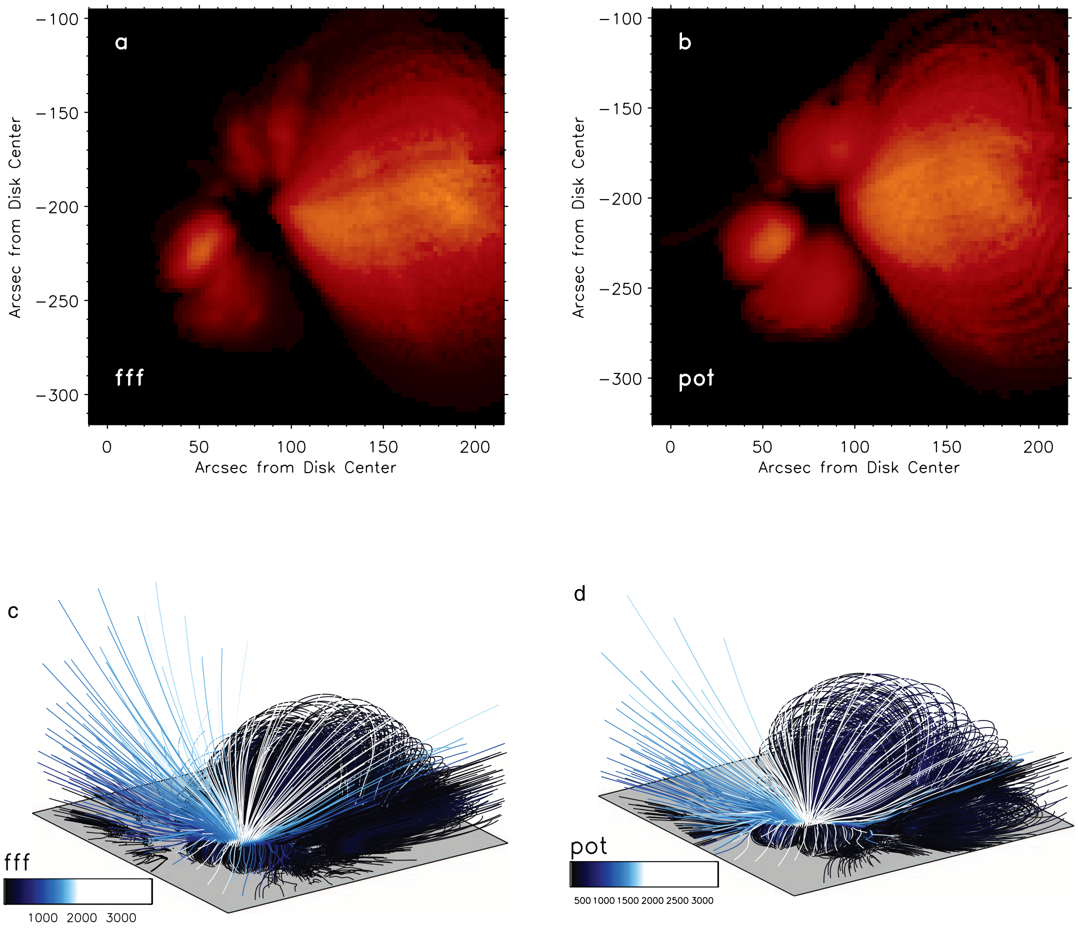

Fig. 13.—Comparison between different magnetic field representations: (*a*) original quasi–force-free field model (fff), same as Fig. 7; (*b*) potential field model (pot); (*c*) field lines from original fff model; and (*d*) field lines from potential field model. Synthetic images use B/L scaling for the heat energy.

plasma emitting in the wavelengths observed by SXT. The filling factor is commonly invoked as an empirical adjustment (fudge factor) to force the total emission from the region to match the observed emission in two different filters. Here, we will test this filling-factor approach for computing forward models of AR 8210 using our four proposed scaling relationships for coronal heating.

Presently, our heating proportionality constant is chosen to match the total emission in one filter, chosen for its proximity in time to the time of the magnetogram data. Rendering the same model active region as viewed through a different filter but with the same proportionality constant produces an image whose total emission does not match the observations, resulting in discrepancies in the filter ratio temperature and emission measure values. Here we explore a different approach where we choose the proportionality constant to match the *temperature* of the observations. We subsequently calculate a filling factor, f required to scale the synthetic emission measure, $\mathrm{EM_{synth}}$, to exactly equal the observed emission measure, $\mathrm{EM_{obs}}$,

$$f = \frac{\mathrm{EM_{obs}}}{\mathrm{EM_{synth}}}. \tag{19}$$

We multiply the final emissions by this factor.

Figure 14 shows the images resulting from this method, and Table 4 shows the resulting filling factors and heating proportionality constants, along with quantitative comparisons with the observations. These filling factors are calculated using observations in the thin Aluminum (Al.1) and Dagwood sandwich

TABLE 3

AR 8210 Magnetic Field Model Comparison

Magnetic Field Model	C	r	s	σ	log (T)	log (EM)
fff	8.3×10^4	0.11	0.52	2.3	6.48	48.71
Potential	8.3×10^4	0.19	0.57	2.4	6.46	48.84
Double no. of field lines	8.3×10^4	0.12	0.50	2.4	6.48	48.72
Equally spaced field lines	8.3×10^4	0.14	0.51	1.8	6.47	48.61
Observed	. . .	1	1	0	6.60	48.30

Notes.—This table shows effect of changing the magnetic field model on prediction accuracy. Nonlinear quasi–force-free field model (fff) and potential field (potential) extrapolations are shown, as well as the quasi–force-free model with double the number of field lines (double no. of field lines) and with equally spaced field lines (equally spaced field lines).

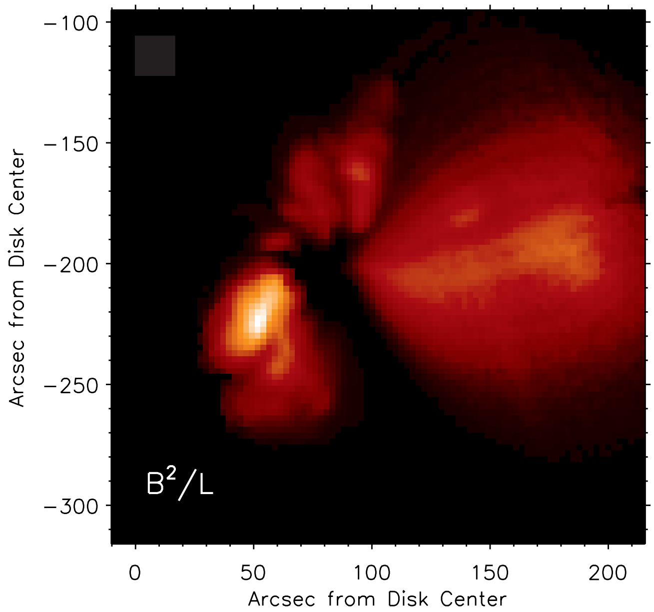

Fig. 14.—Synthetic SXT images of AR 8210 with B^2/L heating, created using the filling factor technique to determine the amount of heat deposited in the corona. Filling factor is calculated using emission in the thin Aluminum (Al.1) and Dagwood sandwich (AlMgMn) filters, at times 19:39:49 and 19:40:53.

(AlMgMn) filters, at times 19:39:49 and 19:40:53. We find substantial difference in some of the synthetic images, such as the B/L example.

The filling factors we find necessary to match single temperature filter ratios for AR 8210 are small (0.01–0.05) for the four scaling relationships we consider. These values are somewhat smaller than those previously found in the corona. Typically reported coronal filling factors lie between about 0.1 and 1.0 (e.g., Winebarger et al. 2003; Aschwanden et al. 2003; Schrijver et al. 2004; Landi & Landini 2004; Ugarte-Urra et al. 2005), although Porter & Klimchuk (1995) found filling factors as low as 10^{-3} for SXT loops. However, many of these authors have focused on individual loops, which may yield different filling factors than our attempt to model an entire active region.

Because of the small filling factors and also because it is more directly related to the observed data, our position is that choosing the proportionality constant by matching the total emission in a selected bandpass is most appropriate for our coronal heating study. With this method, we can ask the question, "If we adjust the total heat deposited to match the emission in one filter, which model assumptions best match the emission in the other filters?" Temperature and emission measure diagnostics allow us to quantitatively compare the answer to this question from different model runs. In contrast, the filling factor method forces agreement in both filters by matching the temperature, invoking a "fudge factor" to explain the resulting difference in emission measure.

6.2. *Heating Scale Height*

Another assumption in our loop model is that loops are heated uniformly throughout their volume. Priest et al. (2000) originally pointed out that some coronal heating theories predict different distributions of heat with respect to loop height. This has inspired a number of authors to look for an observed trend in loop temperature profiles that could indicate a preferred heating distribution, with widely varying results. One particularly oft-cited *Yohkoh* loop was found by different authors to have uniform heating (Priest et al. 2000), heating concentrated at the loop footpoints (Aschwanden 2001), and heating concentrated at the apex (Reale 2002). In this section, we study the effects of varying the distribution of heat energy with height.

We invoke the following functional form for heating function, E_H:

$$E_H = E_{H0} e^{-s/s_H}, \tag{20}$$

where E_{H0} is the uniform heating value through the loop (such as $E_{H0} = C\bar{B}/L$ in the case with B/L scaling), s is the loop length distance from the footpoint, and s_H is a heating scale height.

Our original loop model uses a very large heating scale height, $s_H = 10^{15}$ cm, resulting in effectively uniform heating. In this case, we choose values for s_H that are closer in size to typical loop length values, which in this case lie between about 2×10^8 and 3×10^{10} cm. Figure 15 shows a few examples of synthetic images produced with positive (footpoint heating) and negative (apex heating) scale heights. Table 5 shows the diagnostics for these cases.

We find that heat concentration at the loop apex increases the temperature while decreasing the emission measure, bringing both our temperature and emission measure diagnostics closer to the observed value. A scale height between -10^9 and -10^{10} cm is required to bring the synthetic temperature to match the observed temperature. Conversely, a heat concentration at the footpoints increases emission measure and decreases temperature, bringing both values further away from the observed quantities.

On the other hand, concentrating heat at the footpoints brings the synthetic image closer in appearance to the observations, while

TABLE 4

Filling Factor Comparison

Scaling	C	r	s	σ	log (T)	log (EM)	f
B/L	3.3×10^5	0.22	0.55	1.5	6.59	48.30[a]	5.6×10^{-2}
B/L^2	3.3×10^{15}	0.37	0.62	1.7	6.58	48.30[a]	1.3×10^{-2}
B^2/L	1.4×10^3	0.31	0.55	1.3	6.59	48.30[a]	5.3×10^{-2}
B^2/L^2	5.2×10^{12}	0.27	0.58	2.5	6.58	48.30[a]	3.2×10^{-2}
Observed	...	1	1	0	6.60	48.30	...

Notes.—Comparison table for images in Fig. 14 , created with filling factor method of § 6.1. Table includes heating proportionality constant C, Pearson correlation coefficient, r, Spearman rank correlation coefficient, s, intensity-weighted rms relative error, σ, log of single temperature and emission measure values, T and EM, respectively, and filling factor, f. Comparison values are all relative to observations. Units of C vary, but are always such that C times the scaling relationship is equal to the volumetric heat flux in units of ergs cm^{-3} s^{-1}. The T values are expressed in kelvins, and EM values are expressed in cm^{-3}. All other values are unitless.

[a] These values are adjusted using the filling factor to match the observed emission measure.

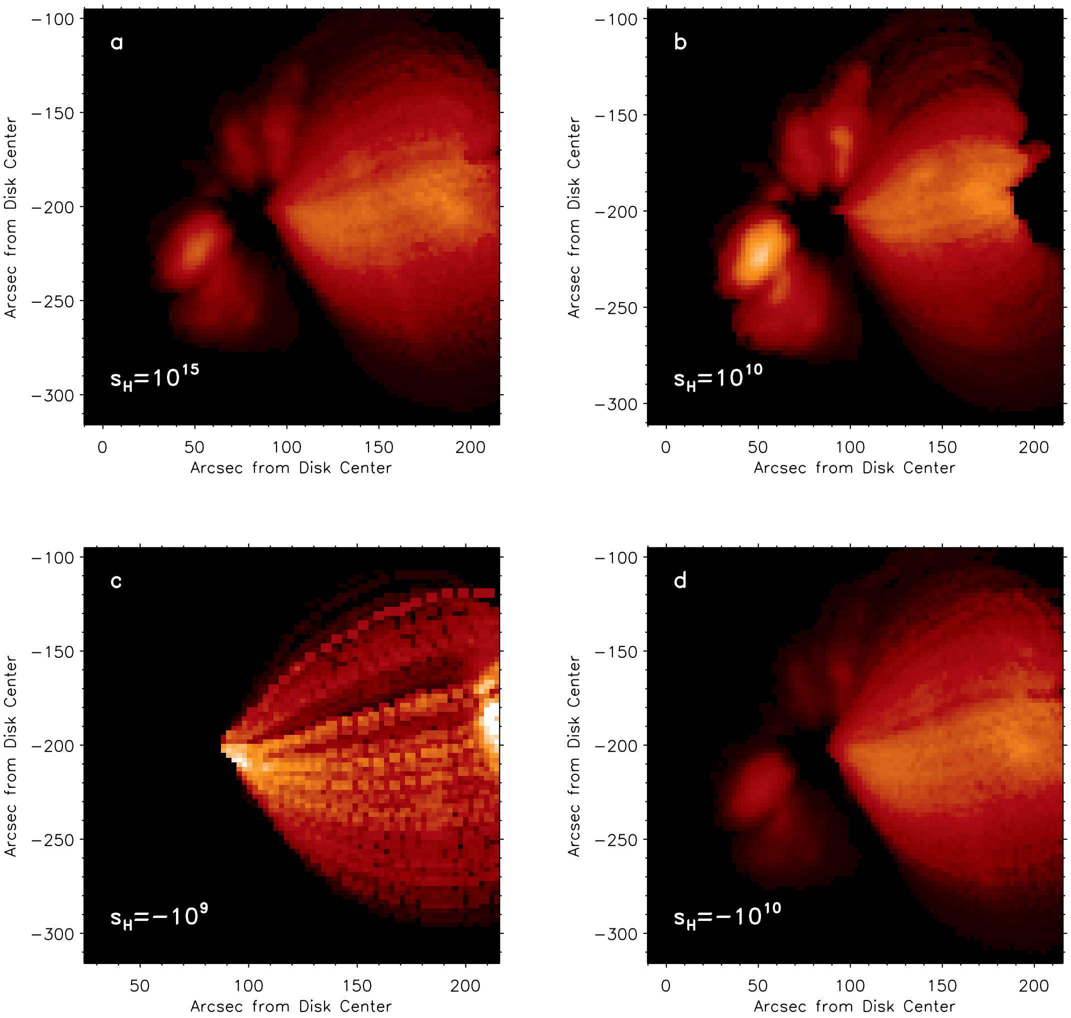

FIG. 15.—Four synthetic SXT images of AR 8210, with heating that scales as *B*/*L*, using four different heating scale heights: (*a*) 10^{15} cm, (*b*) 10^{10} cm, (*c*) -10^{9} cm, and (*d*) -10^{10} cm. First panel with $s_H = 10^{15}$ cm is the original image, with effectively uniform heating. Smaller positive values of s_H represent heating concentrated at the footpoints, while negative values represent heating concentrated at the apex.

apex heating results in reduced image prediction quality. A scale height of 10^{10} cm improves the correlation coefficient markedly, and brings the weighted rms relative error down by nearly 20%. In contrast, a scale height of -10^{10} cm brings the correlation coefficient down and the weighted relative error up by about 25%, and a scale height of -10^{9} cm increases it by over 200%.

TABLE 5
HEATING SCALE HEIGHT COMPARISON

s_H	C	r	s	σ	log (T)	log (EM)
1×10^{15}	8.3×10^{4}	0.11	0.52	2.3	6.48	48.71
1×10^{10}	1.5×10^{5}	0.30	0.61	1.9	6.47	48.79
-1×10^{9}	6.1×10^{1}	−0.05	0.32	7.7	6.71	48.23
-1×10^{10}	5.3×10^{4}	0.05	0.49	2.9	6.51	48.66
Observed	...	1	1	0	6.60	48.30

NOTES.—Comparison table for images in Fig. 15 . All values are for heating that scales as *B*/*L*. Table includes scale height s_H, heating proportionality constant *C*, Pearson correlation coefficient, *r*, Spearman rank correlation coefficient, *s*, intensity-weighted rms relative error, σ, and log of single temperature and emission measure values, *T* and EM, respectively. Comparison values are all relative to observations. The units of s_H are centimeters. Units of *C* vary, but are always such that *C* times the scaling relationship is equal to the volumetric heat flux in units of ergs $\mathrm{cm}^{-3}\ \mathrm{s}^{-1}$. The *T* values are expressed in kelvins, and EM values are expressed in cm^{-3}. All other values are unitless.

Unfortunately, changing the heat distribution with height in this way changes the way the total heat deposited in the loop scales with loop length,

$$\int_0^L E_H\, ds \propto E_{H0} s_H e^{-L/s_H}. \tag{21}$$

Thus, the differences in image prediction quality may be a result of changing the form of the heating relationship rather than merely the distribution of heat within a loop. With a scale height of -10^{9} cm, the effect is so dramatic as to cause the short loop on the left portion of the image to reduce in temperature so much as to disappear from view in SXT (when the total emission is adjusted to match the observed emission).

From these results, there is no clear conclusion as to whether footpoint or apex heating should be employed. Footpoint heating improves the synthetic image fit but worsens the temperature fit. Apex heating worsens synthetic image fit but improves temperature fit. Thus, we use uniform heating in further calculations.

6.3. *Elemental Abundances*

Our assumptions for elemental abundances are taken from the Fludra & Schmelz (1999) model (see Appendix A for more information). Revising these assumptions to a greater abundance

TABLE 6

Coronal Abundance Comparison

Model	Fe Abund.	C	r	s	σ	log (T)	log (EM)
Fludra[1]	6.76×10^{-5}	8.3×10^4	0.11	0.52	2.3	6.48	48.71
Feldman[2]	1.26×10^{-4}	8.3×10^4	0.11	0.52	2.3	6.48	48.49
Meyer[3]	3.89×10^{-5}	8.3×10^4	0.13	0.52	2.3	6.47	48.94
Observed	. . .	. . .	1	1	0	6.60	48.30

Notes.—Comparison table showing the effect of varying elemental abundances. All values are for heating that scales as B/L. Table includes abundance model, iron abundance, heating proportionality constant C, Pearson correlation coefficient, r, Spearman rank correlation coefficient, s, intensity-weighted rms relative error, σ, and log of single temperature and emission measure values, T and EM, respectively. Comparison values are all relative to observations. Abundances are all relative to hydrogen and are taken from the CHIANTI atomic database. Units of C vary, but are always such that C times the scaling relationship is equal to the volumetric heat flux in units of ergs cm^{-3} s^{-1}. The T values are expressed in kelvins, and EM values are expressed in cm^{-3}. All other values are unitless.

References.—(1) Abundances from Fludra & Schmelz (1999). Additionally includes Li, Be, B, F, Sc, V, Mn, Co, Cu from Grevesse & Sauval (1998) with high-FIP abundances decreased by a factor of 1.3 and low-FIP abundances increased by a factor of 2.09 for consistency with Fludra & Schmelz (1999). (2) Abundances from Feldman et al. (1992). Additionally includes K abundance of Landi et al. (2002) and Li, Be, B, F, P, Cl, Sc, Ti, V, Cr, Mn, Co, Cu, and Zn abundances from Grevesse & Sauval (1998) with low-FIP elements increased by a factor 3.5 for consistency with Feldman (1992). (3) Coronal abundances from Meyer (1985).

value for iron, which dominates X-ray coronal emissions, would increase total emissions at a given temperature. Because our method matches total emissions, this yields increased temperature and decreased emission measure, while keeping total emissions the same.

The Feldman (1992) model, due to different assumptions regarding the first ionization potential (FIP) effect, predicts higher coronal iron abundances. Table 6 shows the effects of these different assumptions, as well as the iron abundances for each model. For completeness, we also include a third model which predicts lower iron abundances (Meyer 1985).

We find that there is negligible difference between the synthetic images created using the different assumptions for elemental abundances in the corona, but there is substantial difference in the predicted emission measure values. The reason for this behavior is easy to understand. Changing the abundance of iron is tantamount to changing the level of the plasma emissivity. Yet the total radiative output of the active region is constrained to match the observed value. If the iron abundance is decreased, the emission measure must increase by a similar amount to compensate for the reduced emissivity in achieving energy balance. Thus, the emission measure for the Feldman model (higher coronal iron abundance) is lower by ~40%, while the temperature is increased by less than 0.3%. With the Meyer model (lower coronal iron abundances), the emission measure is increased by ~80% and the temperature is decreased by ~5%. We note that each of these cases use the same proportionality constant in the heating function $E_H = C\bar{B}/L$. Recall that our model requires the total predicted emission to match the observed total emission to within 5%. Each of these cases lies within that window, but they do not have the same total emission. The emission decreased by ~2% for the Feldman model and increased by ~0.6% for the Meyer model. This results in small changes to the temperature and emission measure values, so the changes in those quantities reported here should be seen only as rough approximations.

6.4. *Thermal Conduction*

Another assumption that might affect temperature prediction is a departure from the Spitzer (1962) approximation to the thermal conductivity. There are indications that the Spitzer (1962) approximation may be inaccurate, at least at times, in the solar corona (e.g., Phillips et al. 2005), which would change the temperature and density results. An increase in the thermal conductivity would decrease the temperature, and vice versa.

Although alternatives to the Spitzer conductivity would take a different form than what we have assumed for F_C ($\boldsymbol{F}_C = -\kappa_0 T^{5/2}\nabla T$), we can perform a simple adjustment of the parameter κ_0 in this equation to investigate the effects of increased or decreased thermal conductive flux on our model results. However, in our model, the effects of changing the coefficient κ_0 are equivalent to changing the proportionality constant C in heating parameterization. In the static solution (Rosner et al. 1978), the loop apex temperature T_A is proportional to $C^{2/7}$ and $\kappa_0^{-2/7}$, and this relationship is approximately correct in our model here. Thus, varying the degree of thermal conductivity to match the observed temperature results in changes to the temperature similar to those discussed in § 6.1.

6.5. *Dynamics*

An important loop modeling issue that could affect the temperature and emission measure is loop dynamics. Unfortunately, the computational time and parameter space required to explore dynamically heated loops throughout an active region is prohibitively large. However, we are able to draw some simple conclusions about the expected effects of dynamically heated loops.

Consider, for example, a single loop undergoing time-dependent heating. As a loop begins to be heated uniformly from a cooled state, its density is initially small, and radiative losses are negligible. Thus the temperature rises quickly, before the coronal density has a chance to increase due to chromospheric evaporation. This behavior is called the strongly evaporative phase, when the temperature increases rapidly to a saturation point very near its steady state equilibrium value, while the density increases linearly with time (e.g., Fisher & Hawley 1990). The energy equation for this loop, ignoring gravity and area variations, will be

$$\tfrac{3}{2}\dot{P} = \langle E_H \rangle, \qquad (22)$$

where $\dot{P}$ is the time derivative of the loop gas pressure. Assuming that the temperature is saturated, the emission measure, EM, is proportional to particle density squared, so we have

$$\mathrm{EM}^* \propto \left(\frac{\langle E_H \rangle t}{3kT}\right)^2, \qquad (23)$$

where the asterisk superscript indicates that this emission measure refers to a single coronal loop, and assuming a filling factor of unity within that one loop. When the heating continues for a long enough time, the density eventually reaches its steady state value. If observed before that time, the observed emission measure $\mathrm{EM}^*_{\mathrm{obs}}$ would be a function of the fraction of time t the loop had been heated, compared to the time that it takes to reach an equilibrium, τ_{eq},

$$\frac{\mathrm{EM}^*_{\mathrm{obs}}}{\mathrm{EM}^*_{\mathrm{eq}}} = \left(\frac{t}{\tau_{\mathrm{eq}}}\right)^2, \tag{24}$$

where $\mathrm{EM}^*_{\mathrm{eq}}$ is the emission measure that would be observed if the loop were in a steady state equilibrium. This timescale,

$$\tau_{\mathrm{eq}} \equiv \frac{3P_{\mathrm{eq}}}{2\langle E_H\rangle}, \tag{25}$$

is typically between 30 and 5×10^4 s for our loops.

Suppose the loops were being heated intermittently for timescales short enough that they never reach an equilibrium phase, but long enough that the temperature saturates (Appendix A of Fisher & Hawley 1990). Then the observed emission measure would likely be dominated by loops in this strongly evaporative phase, because the temperature drops rapidly after the heating ceases (Fisher & Hawley 1990), leaving the evaporating loops as the only loops with temperatures high enough to radiate appreciably in X-ray band passes.

Furthermore, intermittent heating would affect the inferred spatial filling factor. Many of the reported filling factors in the literature cited in § 6.1 are for individual coronal loops (as resolved by our current instruments). As all the intermittently heated loops in an active region may not be heated simultaneously, the effective filling factor would reflect the percentage of loops undergoing heating at any given time. If heating timing is consistent between loops and spread evenly over long time averages, then we could identify a "temporal filling factor" due to these effects,

$$f_{\mathrm{temporal}} \equiv \left(\frac{\tau_{\mathrm{on}}}{\tau_{\mathrm{on}} + \tau_{\mathrm{off}}}\right), \tag{26}$$

where τ_{on} is the time that a given loop is heated, and τ_{off} is the time the heating mechanism is not actively adding energy to the system.

Thus, we would expect the observed emission measure to be reduced by its steady state equilibrium value by the amount

$$\mathrm{EM}_{\mathrm{obs}} = f_{\mathrm{spatial}}\left(\frac{\tau_{\mathrm{on}}}{\tau_{\mathrm{eq}}}\right)^2\left(\frac{\tau_{\mathrm{on}}}{\tau_{\mathrm{on}} + \tau_{\mathrm{off}}}\right)\mathrm{EM}_{\mathrm{eq}}, \tag{27}$$

where f_{spatial} is the spatial filling factor for a single loop. In our model calculations for AR 8210, we find that in order to match observed temperatures, the product of the first three terms in equation (27) must be of order 10^{-2} (see § 6.1).

Of course, this is a very simplified approximation. In reality, time-dependent heating is probably manifested in different timescales on different loops, with time-varying temporal profiles. But this approximation gives us an order-of-magnitude estimate for the types of effects that could reduce the actual emission measure below our measured value as a result of dynamic heating.

7. DISCUSSION AND CONCLUSIONS

We have presented a method for modeling the thermodynamic and radiative properties of an active region. The intention is to build synthetic images to represent the expected coronal emissions. These predictions can be compared with observations in order to test the model assumptions such as parameterized coronal heating mechanisms. Overall, the method provides an easy way to simulate active region thermodynamics without the computational expense of a full MHD simulation. It has many promising applications, including the coronal heating studies to be presented in Paper II, as well as any other endeavors (wave propagation studies, for example), that require three-dimensional coronal temperature and density information for a given active region.

We have also examined the effects of several different assumptions on our method for predicting the emissions of active region coronae. We focused our efforts on NOAA-designated Active Region 8210, a well-studied region with excellent vector magnetogram and coronal X-ray data. We varied the form of the coronal heating function, the method of coronal magnetic field extrapolation, the field line representation of that coronal magnetic field, the spatial filling factor of the plasma emissions, the distribution of heat throughout our model loops, and the coronal elemental abundances. We have also examined methods to quantify the effects of these changes on our model's fit with observations.

7.1. *Comparison with Observations*

Our comparison techniques fall into two categories: single-valued numbers that provide a quantitative measure for the goodness of fit of a particular quantity or characteristic, and images or distributions of quantities that can be compared visually. The goodness-of-fit parameters include the Pearson and Spearman rank correlation coefficients showing the correlation between image pixels, the weighted rms relative error of the pixel predictions, and the single filter-ratio temperature and emission measure values. Indicators that can be compared qualitatively include the visual morphology of predicted coronal emissions, the distribution of pixel intensity, and maps of filter-ratio temperatures and emission measures.

We find that there is a substantial difference in coronal emission morphologies, as well as in temperature and emission measure predictions, between different forms of the coronal heating function. Thus, our technique is a promising method to observationally constrain the form of coronal heating mechanisms (see Paper II.) In particular, we find a substantial difference between the relative emission from two different categories of coronal field structures present in the image of AR 8210: low-lying, strong, short loops on the left vs. longer, weaker loops on the right.

Some features present in the observations are predicted by our model, particularly the presence of three primary lobes of emission as well as a prominent dark lane with a little or no emission extending vertically through the center of the image. This dark lane is aligned atop the sunspot and likely located in the region of a magnetic separatrix or quasi separatrix layer. In our model the lack of emission is partially (although not entirely) due to the presence of open field lines (lines that close outside our model box) within the dark lane of emission. We are not able to model open field lines, so we have no emission in this location. However, open field lines or very long, extended loops are likely to have little emission in any case.

X-ray emissions are often suppressed above sunspots, and one possible explanation may be the common presence of open lines above the sunspot (see e.g., Golub et al. 1990). The presence of open lines in our model, and the predicted dark lane of emission similar in shape and extent to the observations, is consistent with this explanation.

Other features in the observed SXT image are absent from all of our synthetic images. In particular, the leftmost lobe of emission is too small in every model case. This is probably due to the magnetic field representation of the corona. There are no field lines in our extrapolation that extend out widely enough to cover the location of the emission, so no heating mechanism could ever successfully reproduce the morphology of this emission. This is true even when we vary the method of solving for the coronal magnetic field or vary the field line representation of the field.

Our model is only able to consider field lines that close within a three-dimensional cube normal to the surface of the Sun. It is possible that the extended emission on the left portion of the 8210 image is due to loops whose footpoints lie beyond the left boundary of our vector magnetogram data. However, examination of the MDI line-of-sight magnetogram data indicates that there is little or no photospheric magnetic field present immediately beyond the boundary of our magnetogram.

A possible explanation for this discrepancy is that loops on this left side of the region are overly extended beyond a force-free state, ballooned outwards due to some dynamical process. This region produced a number of coronal mass ejections (CMEs) and flares (see, e.g., Warmuth et al. 2000; Pohjolainen et al. 2001; Sterling & Moore 2001a, 2001b; Sterling et al. 2001; Simnett 2002; Wang et al. 2002; Leka & Barnes 2003; Roussev et al. 2004), although we have chosen a time prior to the occurrence of flares as large as M class. Most notably, Sterling & Moore (2001a, 2001b) and Sterling et al. (2001) find the presence of features in the EUV and X-ray movies which they refer to as "EIT crinkles." The pattern involves some unique transient, localized brightening and dynamics occurring repeatedly on the leftmost (east) side of the active region. The loops in the leftmost lobe indeed appear to be brightening and extending in and out in these movies. A similar pattern is visible in the SXT movies. The authors explain these phenomena as the results of an interaction between the active region and a coronal hole located to its west. These dynamics may be responsible for the discrepancy between our force-free coronal magnetic field extrapolation and the observed emissions.

7.2. *Testing Model Assumptions and Parameters*

A primary purpose of this paper has been to examine the effect of some of our assumptions and of varying some of the parameters we are able to adjust. In § 5 we vary some of our assumptions about the coronal magnetic field. We found very little difference between the potential field and our quasi–force-free field extrapolation. This suggests that the computational time required to calculate a force-free or quasi–force-free solution may not be worth the effort. This does not necessarily mean that the potential field is a good approximation, as noted above, we have significant doubts about the accuracy of even our force free extrapolation for this particular region.

Further in § 5 we find little effect when we change our field line representation of the coronal magnetic field. Neither changing the number of field lines that we draw nor the method of choosing field lines to model resulted in substantial changes to the synthetic images.

We have also explored some assumptions used in our loop modeling. In § 6.1 we have considered different options for determining the total amount of heat deposited in a loop, in light of the fact that all of our heating parameterizations underestimate observed temperature and overestimate observed emission measure in this active region. The objective was to choose the proportionality constant from the heating parameterization to match the temperature and to assume that the variation of emission measure could be explained through a volumetric filling factor. We found that the resulting filling factors range from 0.01–0.05, depending on the assumed heating model chosen.

Adjusting the amplitude of the of thermal conductivity appears to have little or no effect, as we find that changing the Spitzer coefficient κ_0 is equivalent to adjusting the proportionality constant *C*, since the model X-ray radiance is constrained to match the observed value.

We similarly attempted to reproduce the observed temperature and emission measure by altering the distribution of heat within the loop. We found that distribution of heating within loops had a substantial impact on the final synthetic image. We were able to reproduce the observed temperature and significantly improve our emission measure prediction by concentrating the heat deposition near the loop apex. However, this improvement comes only at a significant cost in the quality of image morphology prediction. Conversely, heating concentrated at loop footpoints results in improved image morphology representation, but results in poorer temperature prediction.

We considered the effects of our assumed elemental abundances. Increased iron abundance in the corona results in slightly increased temperature and reduced emission measure, although the effect is not large enough in either instance to reproduce the observations. The effects on image morphology are negligible.

Our assumption that coronal loops are steadily heated in AR 8210 is a possible reason that we underestimate temperatures for all the heating models we considered. Our model can provide constraints on the heating if we extend the concept of a "filling factor" to represent the fraction of both time and space that plasma is heated. We find that for a corona consisting of loops heated uniformly but intermittently, the product of (1) a loop spatial filling factor, (2) the square of the ratio of heating time to the time it takes to reach steady equilibrium, and (3) the ratio of heating duration to total time must be $\sim 10^{-2}$.

Thus, we speculate that the inaccuracies in our model predictions for both temperature and emission morphology might ultimately stem from our steady state assumptions, at least for the active region examined here. Regarding emission morphology inaccuracies, some of the heating parameterizations do a relatively good job of predicting emissions to the extent that the magnetic field lines up with the location of emissions. To the extent that they do not, dynamic reconfiguration of the magnetic field via reconnection or explosive events may account for discrepancies. Regarding temperatures, time-dependent heating within individual loops is a likely source of discrepancy from our steady state model. (Our study in Paper II includes some quieter, nonflaring active regions where dynamic effects might be reduced.)

7.3. *Directions for Future Model Improvement*

The discrepancies between the observations and our forward model predictions indicate several options for future extension of our approach. First, our reconstructions would clearly be aided by widening the field of view of the original vector magnetogram measurements and/or improved overlap between the magnetogram measurement and the X-ray emissions. Full-Sun vector magnetograms are expected to be forthcoming from the SOLIS[5] Vector Spectro Magnetograph (VSM; see, e.g., Jones et al. 2002). Likewise, the *Hinode* mission launched in 2006, provides vector magnetogram data from the Solar Optical Telescope (SOT), overlapping with high-resolution, broadband X-ray emission data from the X-Ray Telescope (XRT). The latter set of instruments will guarantee the same line-of-sight between the two data sets, eliminating the lack of overlap between the three-dimensional magnetic field simulation box and the interpolation box, which lies along the line of sight of the X-ray imager (see Paper II for further

---

[5] Solar Optical Long-term Investigations of the Sun.

discussion of this challenge). SOLIS should solve the same overlap problem by extending the range of the coronal field extrapolation to any desired volume on the Earth-facing solar hemisphere. This would have the additional advantage of allowing the simulation of closed loops that we are unable to simulate now because they terminate on the side of our field extrapolation volume.

If the errors in our reconstructed coronal magnetic field are due to the limited spatial extent of the magnetic field observations, then many of our model discrepancies will be solved by the introduction of these instruments in the near future. If, however, the magnetic field differences are due to dynamic effects, with the magnetic field configuration in a non–force-free state or in a state affected by past history, then a three-dimensional MHD model would be necessary to calculate the magnetic field.

Regarding the inaccuracies of our loop model, we have suggested that our primary discrepancies are due to the presence of intermittently heated loops. Simulating a fully dynamic one-dimensional coronal loop at each field line remains relatively computationally expensive at this juncture. Klimchuk et al. (2005), however, suggest a way that these dynamic effects may be approximated with simplified equations that can be solved significantly faster than those of typical one-dimensional hydrodynamic loop models. The incorporation of this type of loop model into an approach like the one we have developed here may significantly improve reconstruction, as well as allowing for the exploration of dynamic parameters, such as the frequency of the impulsive heating.

7.4. *Conclusion Summary*

Overall, we find that our model produces relatively robust results for a range of assumptions and is relatively insensitive to choices about specific techniques for extrapolating the magnetic field and solving the steady state energy balance, at least for AR 8210. It is, however, extremely sensitive to the specific heating parameterization, making it a promising approach to assess steady state coronal heating mechanisms. We pursue this approach in Paper II, but we caution that the results should be taken only in the context of a steady state configuration, which may have limited viability. Future developments, however, remain available to improve our model approach.

L. L. L. appreciates funding from a NASA Graduate Student Research Program Fellowship and DoD MURI grant “Understanding Magnetic Eruptions on the Sun and Their Interplanetary Consequences.” G. H. F. was supported by the same DoD MURI grant, and by NASA through the Heliophysics Supporting Research and Technology Program (award NNG 05-GF65G-3/08), and through the Theory Program (award NNG 05-G144G-04/08). J.M.M. was supported by a grant from the Solar, Heliospheric and Interplanetary Environment (SHINE) group. We thank K. D. Leka for processed magnetogram data and constructive comments. We thank W. Abbett, B. Welsch, D. Bercik, and T. Metcalf for many helpful discussions.

APPENDIX A

RADIATIVE LOSSES, SYNTHETIC SPECTRA, AND INSTRUMENT RESPONSE CALCULATIONS USING CHIANTI

We calculate the coronal plasma’s optically thin radiative losses using the CHIANTI atomic database, version 4.2 (Dere et al. 1997; Young et al. 2003). For consistency, we use the same database and assumptions to calculate the intensity spectrum of the plasma for comparison with coronal imager data. The CHIANTI options used to calculate the radiative losses and the spectra and are listed in Table 7.

In the AR 8210 example discussed in this paper, where our results are compared with SXT observations, our use of CHIANTI to calculate spectra is equivalent to using a different instrumental response function than that typically employed in SXT analyses. We discuss these differences and their implications in Appendix A1.

Our CHIANTI spectral calculations yield output in the form of a specific intensity spectrum for each temperature value in the temperature range found in our loop solutions. These data can be used to simulate what it would be like for the relevant satellite imager to image our model active region. This procedure is described in Appendix A2.

A1. SXT TEMPERATURE RESPONSE

Our choice of atomic physics assumptions listed in Table 7 and our use of the CHIANTI database for spectral calculations is different than those used in “standard” SXT analyses (i.e., those included in SolarSoft, or those published in Morrison 1994). The most dramatic effect comes from the choice of elemental abundances and ion fractions in ionization equilibrium. As shown by, e.g., Schmelz et al. (1999) temperature and emission measure calculations can be significantly affected by these choices. The default synthetic spectrum used for SXT analyses as published in Morrison (1994) uses abundances from Meyer (1985) and ionization equilibria from Arnaud & Rothenflug (1985). The spectra are calculated using the MEWE_SPEC software package, based on the model of Mewe et al. (1985, 1986). We have chosen more recent results for each of these data sets, as described in Appendices A1.1 and A1.2. Figure 16 shows the effect of these different atomic physics assumptions on the SXT AlMgMn filter response curve. Figure 17 shows the final response function for each SXT filter, with the assumptions listed in Table 7.

A1.1. *Elemental Abundances*

The Meyer (1985) data used in the Morrison (1994) calculation of the SXT response have coronal abundances for elements with a high first ionization potential (FIP) depleted by about a factor of 4 below their photospheric values. A more recent model of coronal composition maintains the same ratio between the high-FIP and low-FIP elements, but has low-FIP elemental abundances enhanced by about a factor of 4 relative to their photospheric values (Feldman 1992; Feldman et al. 1992). The relative abundances of low- and high-FIP elements are approximately the same in the two models, but the absolute abundances (relative to hydrogen) are different, which can have a noticeable effect on emission measure calculations.

We have chosen the most recent model of Fludra & Schmelz (1999), which represents a “hybrid” model in which there is both an enhancement of low-FIP abundances (by about a factor of 2 relative to photospheric values) *and* a depletion of high-FIP abundances (also by about a factor of 2). We have chosen this model because it represents a “compromise” between the two models cited above, and

TABLE 7

CHIANTI Options for Atomic Physics Calculations

CHIANTI Field	Input
Wavelength Range	1–1000 Å
Constant Density	1×10^{10} cm^{-3}
Ionization Fraction	mazzotta_etal_ext.ioneq[a]
All Ions?	Yes
All lines?	Yes
Isothermal?	Yes
log T (K)	4.0–8.0
log EM (cm^{-5})	27.0
Photoexcitation?	No
Units	Ergs
Protons?	Yes
Wavelength Range	1 to 1000 Å
Bin Size	0.1 Å
Instrumental full width at half-maximum	0.5 Å
Continuum?	Yes
All lines?	Yes
Abundances	sun_coronal_ext.abund[b]
Min Abundance	4.37×10^{-11}
Effective Area File	No
Units	Ergs

Notes.—The top section of table lists options for calculating line intensities, and the bottom section lists options for calculating spectra. All options are from the input fields of the CHIANTI `ch_ss` graphical interface. Radiative losses were calculated with the same assumptions, using the `rad_loss` command.

[a] Includes Mazzotta et al. (1998) ionization equilibria values for all elements from H to Ni, plus data for Cu and Zn from Landini & Fossi (1991).

[b] Includes all abundance values from Fludra & Schmelz (1999) augmented by Li, Be, B, F, Sc, V, Mn, Co, and Cu abundance values from Grevesse & Sauval (1998). The Grevesse & Sauval values have been scaled to mimic the "hybrid" FIP effect of Fludra & Schmelz: high-FIP abundances have been decreased by a factor of 1.3, and low-FIP abundances have been increased by a factor of 2.09.

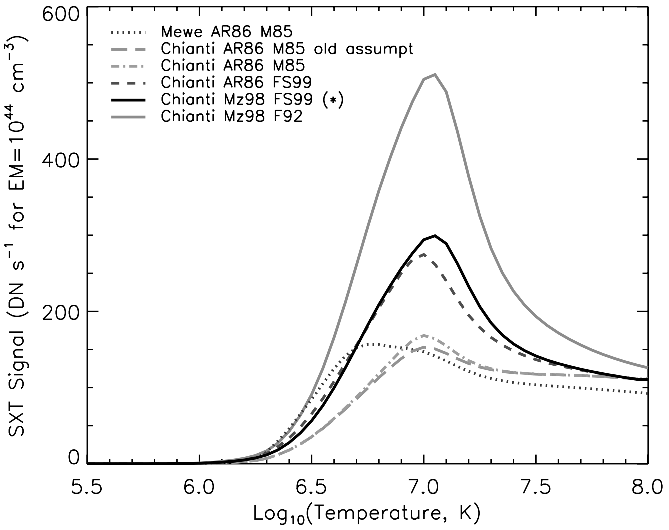

Fig. 16.—Response functions for the AlMgMn filter on *Yohkoh* SXT, calculated using different assumptions. Original response calculated with MEWE_SPEC is shown with the dotted line. Other lines are calculated with CHIANTI, using different assumptions for the ionization equilibrium values: AR85 (Arnaud & Rothenflug 1985) or Mz1998 (Mazzotta et al. 1998) and different assumptions for the coronal elemental abundances: M85 (Meyer 1985), FS99 (Fludra & Schmelz 1999), or F92 (Feldman et al. 1992). There is also a line calculated with CHIANTI that uses as many of the same assumptions as the MEWE_SPEC software as possible (labeled "Chianti AR85 M85 old assumpt"). It uses the same ionization equilibrium and abundance values as Mewe et al., but ignores proton excitation and ignoring the lines in CHIANTI based only on theoretical calculations (as opposed to experimental results). The solid black line labeled with an asterisk, Mz98 FS99 (*) is the response we use in our calculations. [*See the electronic edition of the Supplement for a color version of this figure*.]

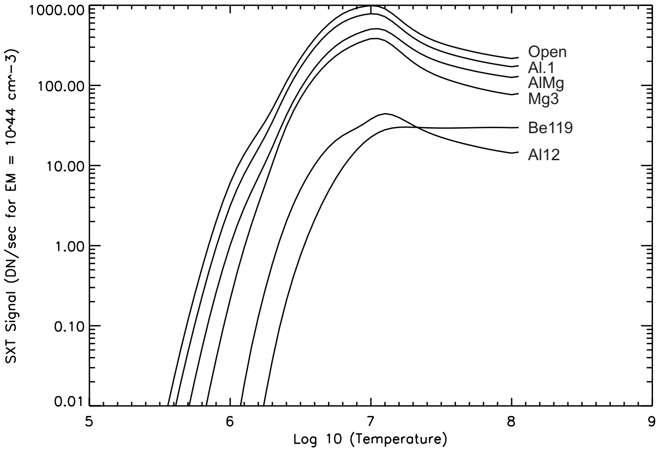

FIG. 17.—Temperature response for *Yohkoh* SXT filters calculated using CHIANTI 4.2.

it appears to fit well with a number of coronal data sets (as opposed to solar wind data sets), such as the flares analyzed by *Yohkoh* BCS in Fludra & Schmelz (1999). We have used a set of abundances built into CHIANTI which includes the Fludra & Schmelz data, plus additional elements with abundances calculated by Grevesse & Sauval (1998) (Li, Be, B, F, Sc, V, Mn, Co, and Cu). These values have been scaled to mimic the "hybrid" FIP effect of Fludra & Schmelz: high-FIP abundances have been decreased by a factor of 1.3, and low-FIP abundances have been increased by a factor of 2.09.

A1.2. *Ionization Equilibria*

We have chosen the most recent ion fractions (assuming ionization equilibrium) data built into CHIANTI 4.2, calculated by Mazzotta et al. (1998). These data incorporate the newest observational results and theoretical calculations. In particular, they include a correction to a known error in the ionization balance calculation for iron which is present in the Arnaud & Rothenflug (1985) data (see, e.g., Arnaud & Raymond 1992). The differences in the Fe ion fractions significantly affect the SXT temperature response functions, as can be seen in Figure 16. In particular, the effects of several iron lines in the range of log $T = 6.2$ through 6.8 are prominent. The Mazzotta et al. data are supplemented with Cu and Zn ionization equilibrium calculations from Landini & Fossi (1991).

A1.3. *Other Model Discrepancies*

It is clear from Figure 16 that there are significant differences between the response function from Morrison (1994) and that calculated with CHIANTI, even when we use the same elemental abundances, ionization equilibrium ion fractions and ignore effects such as proton excitation. This is likely due to different spectral lines intensities between MEWE_SPEC vs. CHIANTI. There are certainly some lines that are included in CHIANTI and not in the Mewe et al. (1985) list. However, in the range of log $T = 6.2$–6.8, the response calculated with Mewe et al. (1985) values is larger than that calculated with CHIANTI, so this discrepancy cannot be the result of extra lines in CHIANTI. At temperatures of log $T = 6.65$, where the discrepancy is largest, the lines that dominate in CHIANTI are Fe XVII and Fe XVIII, in the 10–15 Å range. Thus, we speculate that the differences probably stem to differences in the intensities calculated in this range.

A2. SYNTHETIC IMAGE CREATION

The output from the CHIANTI spectral calculations is a specific intensity I as a function of wavelength λ for each temperature value T, with units of ergs s^{-1} cm^{-2} sr^{-1} Å^{-1}. As noted in Table 7, the spectra are calculated for an emission measure of 10^{27} cm^{-5}, but this assumption is later corrected to reflect the actual emission measure, as shown below.

To create a synthetic image, we need to convert the spectral intensities from CHIANTI to data comparable to that from our chosen coronal imager. The conversion proceeds as

$$D(T, n_e) = 4\pi \frac{A_{\rm pixel} t_{\rm exp} f_{\rm conv}}{\phi_{\rm orig}} \int_{\rm LOS} dz\, n_e^2 \left\{ \int_0^\infty d\lambda \left[\frac{A_{\rm eff}(\lambda)}{4\pi d_{\rm im}^2}\right] I(\lambda, T) \right\}, \tag{A1}$$

where D, as a function of temperature T and wavelength λ, is in the same units as data from the imager (typically DN pixel^{-1} exposure^{-1}). The term $A_{\rm pixel}$ is the area of the imager pixels on the Sun, $\phi_{\rm orig}$ is the assumed emission measure for the spectrum calculation (10^{27} cm^{-5} in our case), $t_{\rm exp}$ is the exposure time of the image, $f_{\rm conv}$ is the appropriate factor for converting energy in ergs to energy in DN for the imager ($\sim 1.71 \times 10^9$ DN ergs^{-1} for SXT), $A_{\rm eff}(\lambda)$ is the effective area of the filter as a function of wavelength, and $d_{\rm im}$ is the distance between the Sun and the imager.

The emission measure integral over the z coordinate in equation (A1) is performed over the line of sight of the imager. Since our interpolation to a three-dimensional grid is done in such a way the data cube is oriented normal to the line of sight of the imager, this integral becomes a simple sum over the z-direction of the data cube. The result of this calculation is a prediction of the DN to be recorded at each imager pixel for a given exposure. These values are then compared with the actual DN recorded at each pixel in the observations.

APPENDIX B

FLOW VELOCITY DEPENDENCE ON APEX TEMPERATURE DIFFERENCE

In our loop solutions, we find the flow velocity of the loop depends on the difference in apex temperatures between the legs of the static solution. Our best-fit solution gives

$$\zeta \approx \left(-9.6 \times 10^{19}\right) \frac{T_{A2}^{*} - T_{A1}^{*}}{T_{A}^{2}}, \tag{B1}$$

where $\zeta \equiv nv/B$ is related by a constant to the, the mass flux, $\xi \equiv \rho v A$; ζ is a function of loop velocity, T_{A1}^{*} and T_{A2}^{*} are the apex temperatures of the two legs of the loop under static conditions (with no flow velocity), and T_A is the actual apex temperature of the final loop solution. This solution is for a heating rate of $E_H = 10^5 \times \bar{B}/L$.

The above expression can be used for a first guess in flow boundary condition iteration, after an initial calculation of static solutions for each of the two loop legs. We do not know the exact value of T_A prior to completion of the loop calculation, but this can be approximated with an average of the two static apex temperatures, or from the analytic static-loop approximation for the entire loop:

$$T_A \sim \left(\frac{\bar{E}_H \mathcal{L}^2}{4\kappa_0}\right)^{2/7}. \tag{B2}$$

To understand the physical origins of the fit given in equation (B1), we begin by integrating the energy equation (7) from footpoint to loop apex. Terms involving the conductive flux drop out, since there is no heat conduction out either footpoint or loop apex. We ignore the $v(\partial P/\partial s)$ term, which we find to be negligibly small in our active region loop calculations. We further assume that the gas pressure varies little enough throughout our short loops that it may be taken out of the integral. With $\zeta = nv/B$ being constant and $P = 2nk_BT$, we find

$$\int_0^{\mathcal{L}} \left(\frac{E_H}{B} - \frac{E_R}{B}\right) \pm 5\zeta k_B T_A = 0, \tag{B3}$$

where the sign of the $5\zeta k_B T_A$ term differs for the two different legs of the loop. The length, $\mathcal{L}$, over which the integration is performed will differ for each of the two loop legs, as well.

We must solve relationship (B3) for ζ. To do so, we make use of the analogous equation for static loops, for which $\zeta = 0$. The integrals in equation (B3) can be written as averages over the length of the leg. The equivalent equation for static loops is

$$\left\langle \frac{E_H^*}{B} \right\rangle \mathcal{L}^* - \left\langle \frac{E_R^*}{B} \right\rangle \mathcal{L}^* = 0, \tag{B4}$$

where the asterisk (*) is used to denote quantities referring to static loop solutions, and the brackets indicate an average over the loop leg.

The heating is a function of magnetic properties such as field line strength that do not differ between the static and nonstatic solutions. Thus we have $E_{H1}^* = E_{H1}$ and $E_{\mathrm{H}_2}^* = E_{\mathrm{H}_2}$, where the subscripts 1 and 2 refer to the two different loop legs. We make the further assumption that $\mathcal{L}_1^* \simeq \mathcal{L}_1$ and $\mathcal{L}_2^* \simeq \mathcal{L}_2$. With these assumptions, we can express E_R in relation to E_R^*,

$$\left\langle \frac{E_R^*}{B} \right\rangle \mathcal{L} = \left\langle \frac{E_R}{B} \right\rangle \mathcal{L} \pm 5k_B \zeta T_A. \tag{B5}$$

If we assume that the change in the average radiative loss rate on each leg of the loop is much less than the total radiative loss rate, that is,

$$\Delta\left[\left\langle \frac{E_R}{B} \right\rangle \mathcal{L}\right] \equiv \left[\left\langle \frac{E_R}{B} \right\rangle \mathcal{L} - \left\langle \frac{E_R^*}{B} \right\rangle \mathcal{L}\right] \ll \left\langle \frac{E_R^*}{B} \right\rangle \mathcal{L}, \tag{B6}$$

then we may write the change in the average loss rate as

$$\Delta\left[\left\langle \frac{E_R}{B} \right\rangle \mathcal{L}\right] = \frac{\partial}{\partial T_A}\left[\left\langle \frac{E_R^*}{B} \right\rangle \mathcal{L}\right] \Delta T_A, \tag{B7}$$

where $\Delta T_A \equiv T_A - T_A^*$ is the change in apex temperatures between the static loop and the loop with a flow.

To use this equation, we can make use of an estimate for the static value of $\langle E_R^* \rangle$ from Fisher & Hawley (1990)

$$\langle E_R^* \rangle = D \frac{\kappa_0 \left(T_A^*\right)^{7/2}}{\left(\mathcal{L}/2\right)^2}, \tag{B8}$$

where $D \equiv (7/4)[\beta_1/(2-\alpha)]^2$, $\beta_1 \equiv B[(11/4 - \alpha/2)/(2-\alpha), 1/2]$. Here, B represents the β-function and α the approximate relationship between the radiative loss function and the temperature: $\Lambda(T) \approx AT^{\alpha}$, with A being a constant.

Equation (B8) is only valid for loops with no area variations, but we will extend it to loops with area variations by making the approximation that $\langle E_R^*/B\rangle \approx \langle E_R^*\rangle/\langle B\rangle$. With this assumption, we can substitute equation (B8) into equation (B7) to get

$$\Delta\left[\left\langle\frac{E_{R1}}{B}\right\rangle\mathcal{L}_1\right] \simeq \frac{7}{2}E_H\left(\frac{\mathcal{L}_1}{\langle B\rangle}\right)\frac{\Delta T_A}{T_A}, \tag{B9}$$

where we have made use of the relationship $E_H = E_H^* = [4D\kappa_0(T_A^*)^{7/2}]/(\mathcal{L}^2)$.

Equation (B5) tells us that the left-hand side of equation (B9) is equal to $\pm 5k_B\zeta T_A$. Thus, equation (B9) may be solved for ζ,

$$\zeta = \pm\frac{7}{10}\left(\frac{DE_H\mathcal{L}}{k_B\langle B\rangle}\right)\frac{\Delta T_A}{T_A^2}. \tag{B10}$$

This expression can be used to choose a first guess for the velocity of the loops if we make the following substitutions. First, we use equation (B2) to approximate a value for T_A. Next, we assume that $\Delta T_A \equiv T_A - T_A^* \approx \mp(1/2)(T_{A2} - T_{A1})$. Finally, we account for our heating law parameterization for E_H. In this case, we are using $E_H = C\langle B\rangle/L$, where $L = \mathcal{L}_1 + \mathcal{L}_2$ is the total loop length. We make the approximation that $\mathcal{L} \approx L/2$. This gives

$$\zeta = -\frac{7}{40}\left(\frac{C}{k_B}\right)\frac{T_{A2}^* - T_{A1}^*}{\left(T_A^\dagger\right)^2}, \tag{B11}$$

where $T_A^\dagger$ is the approximation for the apex temperature given in equation (B2).

Estimating this numerically, we find that, for $C = 10^5$, we have $\zeta = -1.3\times 10^{20}(T_{A2}^* - T_{A1}^*)/T_A^2$. This is in good agreement with the empirical best fit of equation (B1), particularly given the numerous of approximations that went into the derivation.

Equation (B10) can be used to give a good first guess for ζ. In practice, once a large number of loops have been calculated, empirical relationships such as that in equation (B1) give better results, and this is the relationship we have used in most of our solutions.

APPENDIX C

A FIRST-ORDER CORRECTION TO THE BASE PRESSURE AT THE OPPOSITE LOOP FOOTPOINT

The two footpoint pressures of a coronal loop will not be quite equal to one another when there is a steady state flow from one end of the loop to the other. We perform a first-order correction to the base pressure of the second loop leg in order to achieve pressure continuity at the apex.

The pressure correction is based on the existing discrepancy between the apex pressures from the previous guess. We correct the base pressure by an amount proportional to this discrepancy. In practice, we find that a first-order correction of the following form converges most quickly,

$$P_{B2_{\rm new}} = P_{B2} + \delta P_A * \left(\frac{P_{B2}}{P_{A2}}\right), \tag{C1}$$

where P_{A2} and P_{B2} are the base pressure and apex of the second loop leg, and $\delta P_A = P_{A1} - P_{A2}$, with P_{A1} being the apex pressure of the first loop leg. Applying this correction iteratively typically results in a convergence between the apex pressures of the two loops within a couple of iterations.

This iteration is performed as the innermost loop of three iterative loops constructed to determine the loop boundary conditions. At the onset of calculation, neither the apex pressure nor apex temperature values are continuous at the top of the loop. The outermost loop adjusts the velocity to remove the temperature discontinuity. At this stage, the existing apex pressure discontinuity is dominated by the temperature discontinuity, not by the small second leg base pressure adjustment necessary to account for the effects of the flow velocity. During this part of the calculation, it is not useful to adjust the pressure to be continuous; it is more important to first establish the approximate value of the flow to achieve temperature continuity.

To avoid adjusting the base pressure under these circumstances, we add an additional factor that reduces the correction to the base pressure if the apex pressure gap is large (as it is during these initial stages of the calculation). Our final formulation for the iterative pressure correction is

$$P_{B2_{\rm new}} = P_{B2} + \exp\left(-\frac{\delta P_A}{P_{B2}\sigma^2}\right)\delta P_A * \left(\frac{P_{B2}}{P_{A2}}\right), \tag{C2}$$

where $\sigma \simeq 0.13$ is chosen to reduce the base pressure correction to about 10% of its original value when the difference in apex pressures is about 20%. This adjustment allows for a relatively smooth Newton-Raphson convergence in temperature and loop length values before applying a substantial correction to the base pressure.

Because we do not want to achieve pressure continuity until the end of the calculation, we choose to apply our correction for a fixed number of iterations, rather than applying it iteratively until convergence is achieved at each step. We find that five iterations is enough to achieve final pressure convergence for typically about 99% of loops. Loops that do not achieve pressure convergence are discarded, as described in § 2.2.

REFERENCES

Arnaud, M., & Raymond, J. 1992, ApJ, 398, 394

Arnaud, M., & Rothenflug, R. 1985, A&AS, 60, 425

Aschwanden, M. J. 2001, ApJ, 559, L171

Aschwanden, M. J., Nightingale, R. W., & Alexander, D. 2000, ApJ, 541, 1059

Aschwanden, M. J., & Schrijver, C. J. 2002, ApJS, 142, 269

Aschwanden, M. J., Schrijver, C. J., & Alexander, D. 2001, ApJ, 550, 1036

Aschwanden, M. J., Schrijver, C. J., Winebarger, A. R., & Warren, H. P. 2003, ApJ, 588, L49

Barber, C. B., Dobkin, D. P., & Huhdanpaa, H. 1996, ACM Trans. Math. Software, 22, 469

Barnes, G., Longcope, D. W., & Leka, K. D. 2005, ApJ, 629, 561

Brosius, J. W., Landi, E., Cook, J. W., Newmark, J. S., Gopalswamy, N., & Lara, A. 2002, ApJ, 574, 453

Brosius, J. W., & White, S. M. 2006, ApJ, 641, L69

Canfield, R. C., et al. 1993, ApJ, 411, 362

Cargill, P. J., & Priest, E. R. 1980, Sol. Phys., 65, 251

Craig, I. J. D., & McClymont, A. N. 1986, ApJ, 307, 367

Craig, I. J. D., McClymont, A. N., & Underwood, J. H. 1978, A&A, 70, 1

Del Zanna, G., & Mason, H. E. 2003, A&A, 406, 1089

Dere, K. P., Landi, E., Mason, H. E., Monsignori Fossi, B. C., & Young, P. R. 1997, A&AS, 125, 149

Feldman, U. 1992, Phys. Scr. T, 46, 202

Feldman, U., Mandelbaum, P., Seely, J. F., Doschek, G. A., & Gursky, H. 1992, ApJS, 81, 387

Fisher, G. H., & Hawley, S. L. 1990, ApJ, 357, 243

Fludra, A., & Schmelz, J. T. 1999, A&A, 348, 286

Freeland, S. L., & Handy, B. N. 1998, Sol. Phys., 182, 497

Gary, G. A. 2001, Sol. Phys., 203, 71

Gary, G. A., & Hagyard, M. J. 1990, Sol. Phys., 126, 21

Golub, L., Nystrom, G., Herant, M., Kalata, K., & Lovas, I. 1990, Nature, 344, 842

Golub, L., Zirin, H., & Wang, H. 1994, Sol. Phys., 153, 179

Grevesse, N., & Sauval, A. J. 1998, Space Sci. Rev., 85, 161

Harmon, R., Rosner, R., Zirin, H., Spiller, E., & Golub, L. 1993, ApJ, 417, L83

Jones, H. P., Harvey, J. W., Henney, C. J., Hill, F., & Keller, C. U. 2002, in IAU Colloq. 188, Magnetic Coupling of the Solar Atmosphere Euroconference, ed. H. Sawaya-Lacoste (ESA SP-505; Noordwijk: ESA), 15

Kankelborg, C. C., Walker, Arthur, B. C., I., & Hoover, R. B. 1997, ApJ, 491, 952

Kano, R., & Tsuneta, S. 1996, PASJ, 48, 535

Klimchuk, J. A., Patsourakos, S., & Cargill, P. J. 2005, AGU Abstr. Spring, 14, 03

LaBonte, B. J., Mickey, D. L., & Leka, K. D. 1999, Sol. Phys., 189, 1

Landi, E., Feldman, U., & Dere, K. P. 2002, ApJS, 139, 281

Landi, E., & Landini, M. 2004, ApJ, 608, 1133

Landini, M., & Fossi, B. C. M. 1991, A&AS, 91, 183

Landini, M., & Monsignori Fossi, B. C. 1981, A&A, 102, 391

Leka, K. D., & Barnes, G. 2003, ApJ, 595, 1296

———. 2007, ApJ, 656, 1173

Lenz, D. D. 1999, ApJ, 517, 497

Lenz, D. D., Deluca, E. E., Golub, L., Rosner, R., & Bookbinder, J. A. 1999, ApJ, 517, L155

Lin, H., Kuhn, J. R., & Coulter, R. 2004, ApJ, 613, L177

Lionello, R., Linker, J. A., & Mikic, Z. 2003, in AIP Conf. Proc. 679, Solar Wind Ten, ed. M. Velli, R. Bruno, & F. Malara (Berlin: Springer), 222

Longcope, D. W. 2004, ApJ, 612, 1181

Lundquist, L. L. 2006a, Ph.D. thesis, Univ. California (Berkeley)

———. 2006b, AAS Sol. Phys. Meet., 37

Lundquist, L. L., Fisher, G. H., Leka, K. D., Metcalf, T. R., & McTiernan, J. M. 2005, AGU Abstr. Spring, 14, 02

Lundquist, L. L., Fisher, G. H., McTiernan, J. M., Metcalf, T., & Leka, K. D. 2008, ApJ, 689, in press (Paper II)

Lundquist, L. L., Fisher, G. H., McTiernan, J. M., & Régnier, S. 2004a, in BAAS, 204, 801

———. 2004b, in SOHO Workshop 15, Coronal Heating, ed. R. W. Walsh et al. (ESA SP-575; Paris: ESP), 306

Lundquist, L. L., Fisher, G. H., Régnier, S., Liu, Y., & Abbett, W. P. 2003a, AGU Abstr. Fall, 42, 0509

Lundquist, L. L., Régnier, S., Abbett, W. P., & Fisher, G. H. 2003b, BAAS, 34, 811

Mandrini, C. H., Démoulin, P., & Klimchuk, J. A. 2000, ApJ, 530, 999 (MDK00)

Mariska, J. T., & Boris, J. P. 1983, ApJ, 267, 409

Mazzotta, P., Mazzitelli, G., Colafrancesco, S., & Vittorio, N. 1998, A&AS, 133, 403

Metcalf, T. R., Jiao, L., McClymont, A. N., Canfield, R. C., & Uitenbroek, H. 1995, ApJ, 439, 474

Mewe, R., Gronenschild, E. H. B. M., & van den Oord, G. H. J. 1985, A&AS, 62, 197

Mewe, R., Lemen, J. R., & van den Oord, G. H. J. 1986, A&AS, 65, 511

Meyer, J.-P. 1985, ApJS, 57, 173

Mickey, D. L., Canfield, R. C., Labonte, B. J., Leka, K. D., Waterson, M. F., & Weber, H. M. 1996, Sol. Phys., 168, 229

Mok, Y., Mikic, Z., Lionello, R., & Linker, J. A. 2005, ApJ, 621, 1098

Morrison, M. 1994, *Yohkoh* Analysis Guide, Tech. Rep. LMSC-P098510 (Lockheed Palo Alto Research Laboratory)

Nindos, A., Kundu, M. R., White, S. M., Shibasaki, K., & Gopalswamy, N. 2000, ApJS, 130, 485

Orlando, S., Peres, G., & Serio, S. 1995, A&A, 294, 861

Pallavicini, R., Vaiana, G. S., Tofani, G., & Felli, M. 1979, ApJ, 229, 375

Patsourakos, S., Klimchuk, J. A., & MacNeice, P. J. 2004, ApJ, 603, 322

Peres, G., Spadaro, D., & Noci, G. 1992, ApJ, 389, 777

Phillips, K. J. H., Feldman, U., & Harra, L. K. 2005, ApJ, 634, 641

Pohjolainen, S., Maia, D., Pick, M., Vilmer, N., Khan, J. I., Otruba, W., Warmuth, A., Benz, A., Alissandrakis, C., & Thompson, B. J. 2001, ApJ, 556, 421

Porter, L. J., & Klimchuk, J. A. 1995, ApJ, 454, 499

Priest, E. R., Foley, C. R., Heyvaerts, J., Arber, T. D., Mackay, D., Culhane, J. L., & Acton, L. W. 2000, ApJ, 539, 1002

Reale, F. 2002, ApJ, 580, 566

Régnier, S., Amari, T., & Canfield, R. C. 2005, A&A, 442, 345

Renka, R. J. 1988a, ACM Trans. Math. Softw., 14, 139

———. 1988b, ACM Trans. Math. Softw., 14, 149

———. 1988c, ACM Trans. Math. Softw., 14, 151

Rosner, R., Tucker, W. H., & Vaiana, G. S. 1978, ApJ, 220, 643

Roussev, I. I., Sokolov, I. V., Forbes, T. G., Gombosi, T. I., Lee, M. A., & Sakai, J. I. 2004, ApJ, 605, L73

Sakurai, T. 1982, Sol. Phys., 76, 301

Schmelz, J. T., Beene, J. E., Nasraoui, K., Blevins, H. T., Martens, P. C. H., & Cirtain, J. W. 2003, ApJ, 599, 604

Schmelz, J. T., Nasraoui, K., Richardson, V. L., Hubbard, P. J., Nevels, C. R., & Beene, J. E. 2005, ApJ, 627, L81

Schmelz, J. T., Saba, J. L. R., Strong, K. T., Winter, H. D., & Brosius, J. W. 1999, ApJ, 523, 432

Schrijver, C. J., Derosa, M. L., & Metcalf, T. 2005, AGU Abstr. Spring, 31, 05

Schrijver, C. J., Sandman, A. W., Aschwanden, M. J., & DeRosa, M. L. 2004, ApJ, 615, 512

Schrijver, C. J., et al. 2006, Sol. Phys., 235, 161

Serio, S., Peres, G., Vaiana, G. S., Golub, L., & Rosner, R. 1981, ApJ, 243, 288

Simnett, G. M. 2002, Adv. Space Res., 29, 1493

Spitzer, L. 1962, Physics of Fully Ionized Gases, Physics of Fully Ionized Gases (New York: Interscience)

Steele, C. D. C., & Priest, E. R. 1990, Sol. Phys., 125, 295

———. 1991, Sol. Phys., 132, 293

Sterling, A. C., & Moore, R. L. 2001a, ApJ, 560, 1045

———. 2001b, J. Geophys. Res., 106, 25227

Sterling, A. C., Moore, R. L., Qiu, J., & Wang, H. 2001, ApJ, 561, 1116

Thompson, B. J., Cliver, E. W., Nitta, N., Delannée, C., & Delaboudinière, J.-P. 2000, Geophys. Res. Lett., 27, 1431

Tsuneta, S., et al. 1991, Sol. Phys., 136, 37

Ugarte-Urra, I., Doyle, J. G., Walsh, R. W., & Madjarska, M. S. 2005, A&A, 439, 351

Vourlidas, A., Bastian, T. S., & Aschwanden, M. J. 1997, ApJ, 489, 403

Wallenhorst, S. G. 1982, Sol. Phys., 79, 333

Wang, T., Yan, Y., Wang, J., Kurokawa, H., & Shibata, K. 2002, ApJ, 572, 580

Warmuth, A., Hanslmeier, A., Messerotti, M., Cacciani, A., Moretti, P. F., & Otruba, W. 2000, Sol. Phys., 194, 103

Warren, H. P., & Winebarger, A. R. 2007, ApJ, 666, 1245

Webb, D. F., & Zirin, H. 1981, Sol. Phys., 69, 99

Welsch, B. T., Fisher, G. H., Abbett, W. P., & Regnier, S. 2004, ApJ, 610, 1148

Wheatland, M. S., Sturrock, P. A., & Roumeliotis, G. 2000, ApJ, 540, 1150

Winebarger, A. R., Warren, H. P., & Mariska, J. T. 2003, ApJ, 587, 439

Wragg, M. A., & Priest, E. R. 1981, Sol. Phys., 70, 293

Young, P. R., Del Zanna, G., Landi, E., Dere, K. P., Mason, H. E., & Landini, M. 2003, ApJS, 144, 135